BoNuS Experiment Analysis Note

N. Baillie, P. Bosted, S. Bueltmann, E. Christy, G. Dodge, J. Domingo, R. Ent, H. Fenker, K.A. Griffioen, M. Ispiryan, N. Kalatarians, C. Keppel, S. Kuhn, G. Niculescu, I. Niculescu, S. Tkachenko, V. Tvaskis, W. Melnitchouk, J. Zhang

Contents

List of Figures

List of Tables

Chapter 1

RESULTS

1.1 Introduction

The BoNuS data were analyzed using two different methodologies. In the Ratio Method, events tagged with a spectator proton in the RTPC were sorted into kinematic bins and normalized by the inclusive deuteron scattering events for the same kinematics. In this way, the problems of absolute normalization and CLAS acceptance were handled naturally by always dealing with experimental ratios and world parameterizations of known quantities such as the deuteron and proton cross sections. In the Monte Carlo (MC) Method, the tagged spectator events were compared directly to a Monte Carlo simulation of CLAS with events generated according to a plane-wave impulse approximation (PWIA) spectator model. The MC Method produces ratios of data to the simulation, whereas the Ratio Method uses ratios of tagged data to inclusive data. Therefore, the two methods have somewhat different systematic dependencies and their systematic errors are partially independent. Comparing both methods therefore increases the confidence in the extracted results. Both methods produce consistent results and exemplify the success of the tagging technique to measure the free neutron's structure using neutrons bound in nuclei. They are at least partially independent from each other and have somewhat different systematic effects; therefore, a direct comparison of both methods can increase our confidence that systematic errors are under control.

1.2 The Ratio Method

For the Ratio Method, the experimental quantity of interest is the ratio of ed scattering events tagged by a spectator proton and untagged, corresponding to inclusive ed scattering. Once corrected for backgrounds and efficiency, this tagged to untagged ratio equals the structure function ratio F_2^n/F_2^d, provided that the R structure function for the neutron and the deuteron are reasonably close to each other. In order to reduce the effects of final-state interactions and off-shell effects, the spectator momentum was chosen to be $0.07 < p_s < 0.10$ GeV and the spectator angle with respect to the momentum transfer was chosen to be $\theta_{pq} > 100°$.

1.2.1 Accidentals

Coincidence events with an electron measured in CLAS and a spectator proton measured in the RTPC are confirmed by comparing the position z along the beam line of track origins. Fig. 1.1 shows the spectrum of $z_{\mathrm{CLAS}} - z_{\mathrm{RTPC}}$. The large central peak corresponds to true coincidences, and the background on either side corresponds to accidental electron-proton coincidences. The z distributions for electrons and protons are flat over the 16cm length of the target. Therefore, the convolution of these two distributions gives rise to a triangular background spectrum. By fitting the background and peak, one can characterize the events that fall within and outside of the blue limits. A simple multiplicative factor R_{bg} scales the background events to correspond to the number of accidental coincidences under the peak.

1.2.2 Acceptance and Efficiency

The relative CLAS electron detection efficiency ϵ was determined for bins in Q^2 and W using the ratio of observed inclusive scattering rates off the deuteron compared to the radiated model of Bosted and Christy[5, 4] derived from global fits to the world's data. Fig. 1.2 shows the dependence on W for 4 Q^2 bins. The top graphs (blue) are the inclusive data, the middle graphs (black) are the model, and the bottom graphs (red) are the ratio of the two, which is the relative electron efficiency, $\epsilon(W, Q^2)$, for CLAS (which includes acceptance and luminosity).

For each tagged $d(e, e'p_s)X$ event within the spectator proton cuts both W^* (proper invariant mass; see Eq. **??**) and W (nominal invariant mass for a stationary target) were calculated. The variables W^* and Q^2 define which bin to increment in the $N_{tag}(W^*, Q^2)$ table of

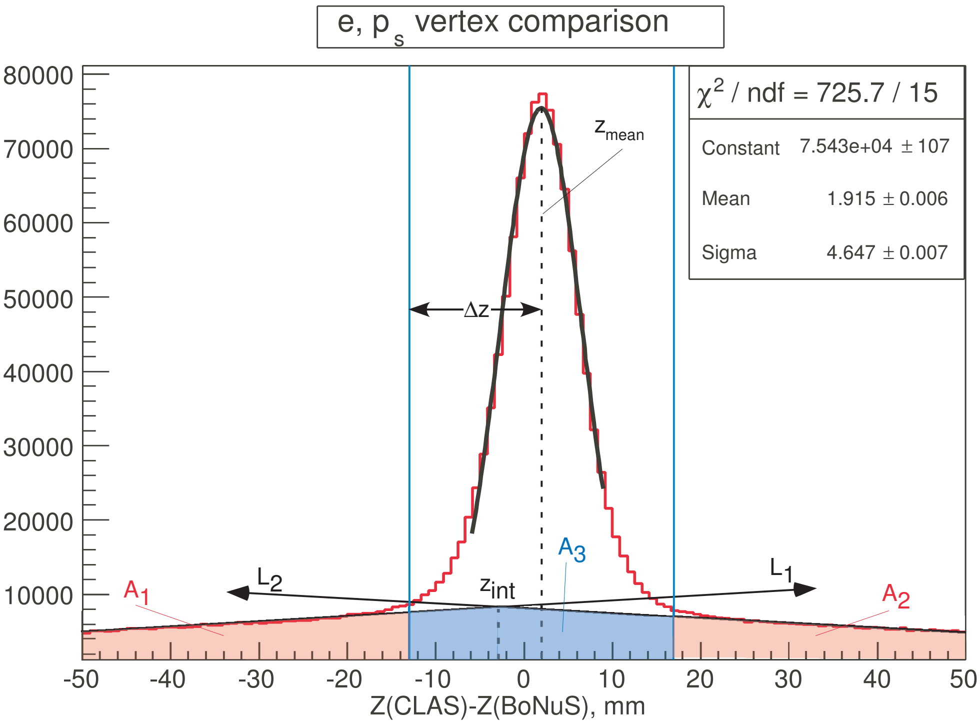

Figure 1.1: Distribution of Δz, the difference between the reconstructed track position along the beam direction of electron and spectator proton. The peak shows coincident events between CLAS and the RTPC. Accidental coincidences appear in the wings.

tagged events. The calculated W and Q^2 determine the efficiency to use. Events are accumulated by adding $1/\epsilon(W,Q^2)$ to the (W^*,Q^2) bin in the tagged table. The corrected ratio of tagged/untagged counts (with the proper subtraction of accidental backgrounds) becomes:

$$R_{corr} = \frac{\sum_{i=1}^{N_{tag}(W^*,Q^2)} \frac{1}{\epsilon_i(W,Q^2)} - R_{bg} \sum_{j=1}^{N_{bg}(W^*,Q^2)} \frac{1}{\epsilon_j(W,Q^2)}}{\sum_{k=1}^{N_{untag}(W,Q^2)} \frac{1}{\epsilon_k(W,Q^2)}} \tag{1.1}$$

In this way, we properly account for the fact that there are several bins in W that contribute to a given W^* bin. Consequently, R_{corr} for an invariant-mass bin $[w_1, w_2]$ contains all tagged events with $w_1 <= W^* < w_2$ in the numerator and all inclusive events with $w_1 <= W < w_2$ in the denominator. In other words, the true invariant mass is used for numerator and denominator.

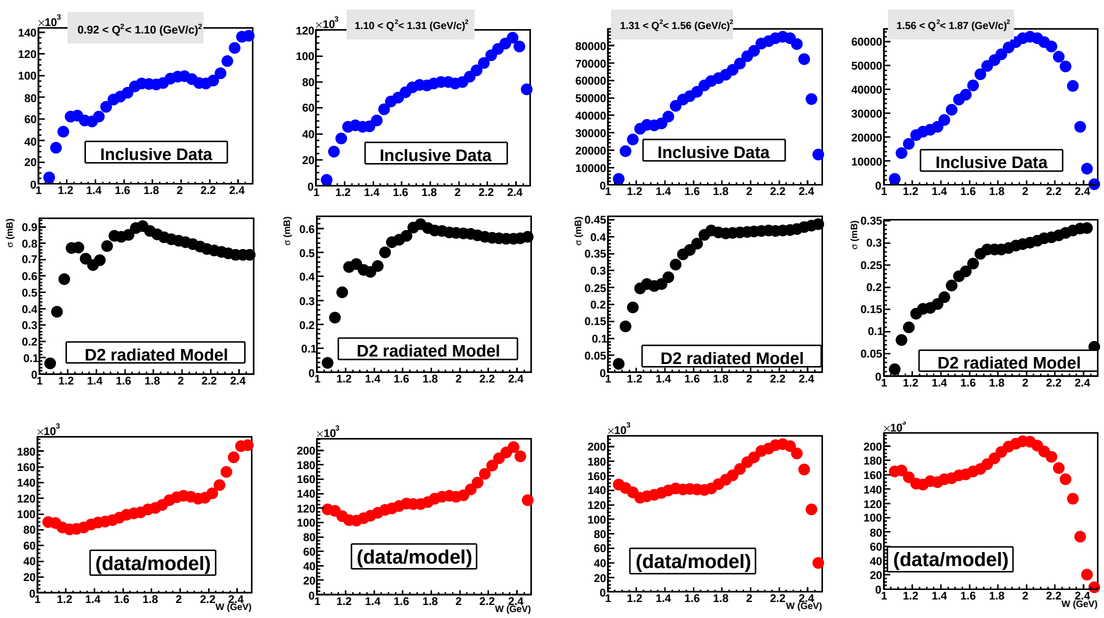

Figure 1.2: The total inclusive electron scattering counts for deuterium (top row), the total radiated deuteron cross section model provided by P. Bosted [5] and E. Christy [4] (middle row) and the ratio of data to model. The plots are all versus invariant mass, W. Each column corresponds to a different Q^2 bin (only the $E_{beam} = 4$ GeV data are shown).

The fall-off at high W for the largest Q^2 value is due to the z and θ cut.

This treatment does not account for the efficiency of the RTPC. J. Zhang's GEANT4 simulation of the RTPC provides us with an acceptance value that is a function of W^*, Q^2, and the spectator kinematics p_s and θ_{pq} (the angle between the spectator proton and the direction of momentum transfer). The acceptance is nearly flat except near the kinematic endpoints. However, because of the difficulty in simulating low-energy ionization within an environment with intense background, the overall RTPC efficiency from the simulation remained uncertain. Consequently, we have devised a way to correct for the RTPC efficiency by normalizing our ratio of tagged/untagged events to the world's cross section ratio data in a kinematic region where σ_n can be extracted from deuteron data without a large dependence on model corrections. We have chosen the DIS region at $x = 0.35$, $W > 2.0$ GeV and $Q^2 > 1.0$ GeV^2. The normalization, simply referred to from now on as n, is found to be $n = 1/0.02535 \pm 3.37\%$, where the error corresponds to the rms variation of n for the multiple Q^2 bins. This was the average value of n obtained from an analysis of the E_{beam} = 4.223 and 5.262 GeV data sets. Fig. 1.3 suggests that n may have a slight Q^2 dependence, but it appears to be small and can be added into the systematic error on the tagged/untagged ratio as a 5% normalization error.

1.2.3 Pion and Charge Symmetric Background Contamination

We have made corrections for pion background and pair symmetric contamination using the CLAS EG1B parameterizations of N. Guler [**?**]. We assume that the EG1B π^-/e^- and e^+/e^- ratios are similar to those of the BoNuS experiment. We use N. Guler's routine to calculate the amount of contamination for each beam energy. We interpolate to our beam energies and use a weighted average of the two ratios r_{NH_3} and r_{ND_3}, for ammonia and deuterated ammonia targets that allows us to extract ratios for the neutron and deuteron. The superscript X represents either π^- or e^+ events, depending on which background we're interested in. The quantity σ_t^X stands for the probability of detecting particle X emerging from target t.

The 10 protons and 8 neutrons in NH_3 and the 10 protons and 11 neutrons in ND_3 lead to the following definitions:

$$r_{NH_3} \equiv \frac{\sigma^X_{NH_3}}{\sigma^e_{NH_3}} = \frac{10\sigma^X_p + 8\sigma^X_n}{10\sigma^e_p + 8\sigma^e_n}, \tag{1.2}$$

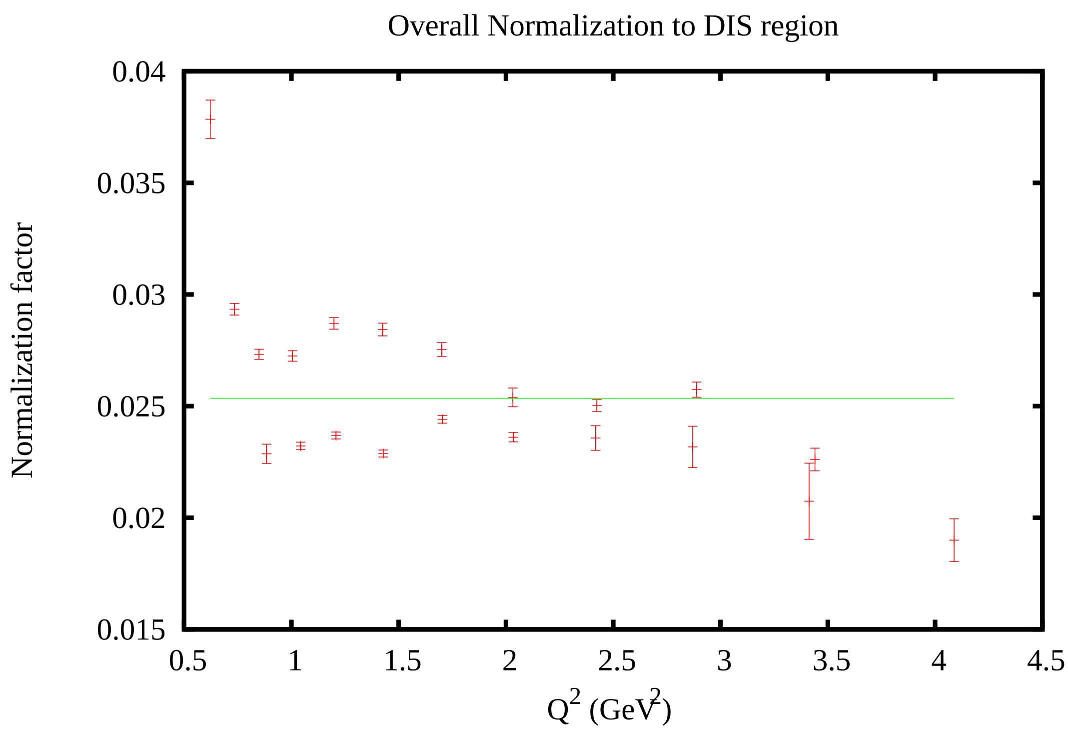

Figure 1.3: The inverse of the overall normalization, n, as a function of Q^2. The green line shows the average value used for the final data set. The plot shows the normalization for the E = 4.223 and 5.262 GeV data sets, which is why there are two points for some of the Q^2 values.

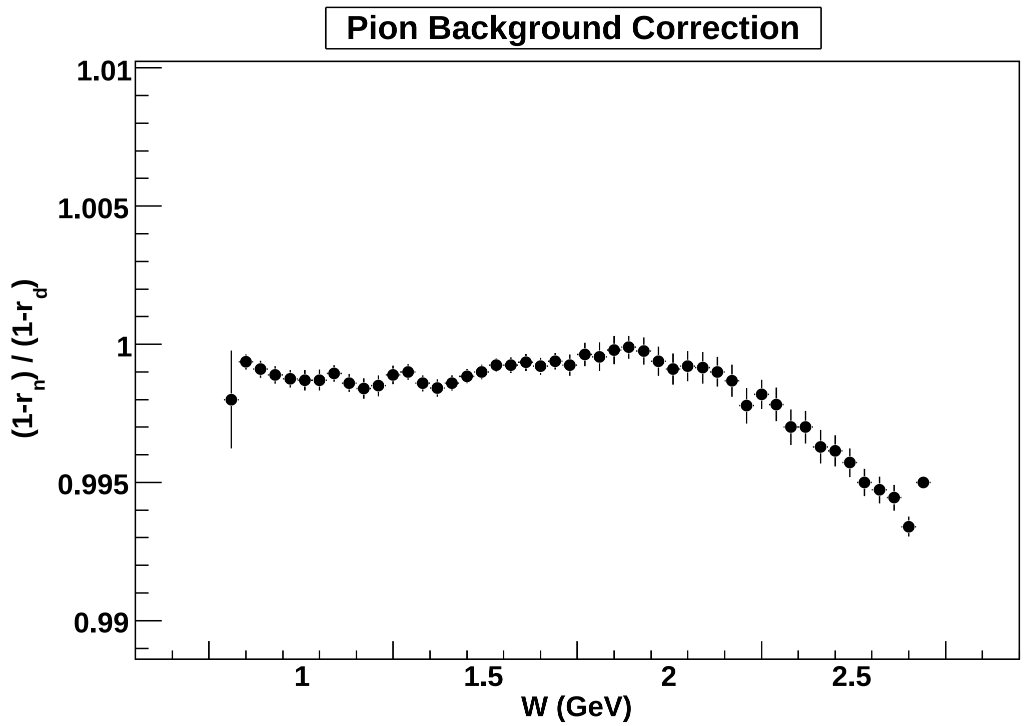

Figure 1.4: The correction to the tagged/untagged ratio due to π^- contamination.

$$r_{ND_3} \equiv \frac{\sigma^X_{ND_3}}{\sigma^e_{ND_3}} = \frac{10\sigma^X_p + 11\sigma^X_n}{10\sigma^e_p + 11\sigma^e_n}. \tag{1.3}$$

For the BoNuS case, we are interested in the contamination ratios for a neutron target (r_n), a deuteron target (r_d), or a proton target (r_p). We use the estimation here that σ_n inside a nucleus equals σ_n for a free neutron. Now we make the following definitions:

$$r_n \equiv \frac{\sigma^X_n}{\sigma^e_n}, r_p \equiv \frac{\sigma^X_p}{\sigma^e_p} \tag{1.4}$$

$$r_d \equiv \frac{\sigma^X_d}{\sigma^e_d} = \frac{\sigma^X_n + \sigma^X_p}{\sigma^e_n + \sigma^e_p} = \frac{Rr_n + r_p}{R+1} \tag{1.5}$$

We've defined $R = \sigma^e_n/\sigma^e_p$ and we use the value for R from P. Bosted's published parameterization of the world's data ([5] and [4]). We can rewrite Eqs. 1.2 and 1.3 as

$$r_{NH_3} = \frac{10\sigma^X_p + 8\sigma^X_n}{(10/R + 8)\sigma^e_n} = \frac{10\sigma^X_p + 8\sigma^X_n}{(10 + 8R)\sigma^e_p}, \tag{1.6}$$

$$r_{ND_3} = \frac{10\sigma_p^X + 11\sigma_n^X}{(10/R + 11)\sigma_n^e} = \frac{10\sigma_p^X + 11\sigma_n^X}{(10 + 11R)\sigma_p^e}. \tag{1.7}$$

The quantities necessary for BoNuS, r_n and r_p, can be expressed as the following linear combinations of the EG1B ratios,

$$r_n = \frac{1}{3}(-(10/R + 8)r_{NH_3} + (10/R + 11)r_{ND_3}) \tag{1.8}$$

$$r_p = \left(\frac{10}{8} - \frac{10}{11}\right)^{-1}\left(\frac{1}{8}(10 + 8R)r_{NH_3} + \frac{1}{11}(10 + 11R)r_{ND_3}\right) \tag{1.9}$$

Now the correction to the BoNuS measured tagged/untagged count ratio is,

$$R_{\text{raw}} = \frac{tagged}{untagged} = \frac{\sigma_n}{\sigma_d} \tag{1.10}$$

$$R_{\text{corr}} = \frac{(1 - r_n)\sigma_n}{(1 - r_d)\sigma_d} = C_X R_{\text{raw}} \tag{1.11}$$

where, as before, $X = \pi$ or e^+. The correction factor, C_X, extracted from EG1B's result for the ratio of π/e is plotted in Fig. 1.4. The correction factor extracted from EG1B's result for the ratio of e^+/e^- is plotted in Fig. 1.5. An attempt was made to estimate just how sensitive the ratio is to the amount of contamination by multiplying r_n and r_p by a factor of 10 and recalculating the correction (Figs. 1.6 and 1.7). The error bars are larger for these figures because they were run over fewer statistics. Even in the extreme case where the contamination from π^- and electron's from e^+e^- pairs is 10 times worse than for the EG1B experiment, it still only introduces a 5% difference in the tagged/untagged ratio at the worst, and in most cases, is less than 1%.

1.2.4 Radiative Corrections

Radiative corrections to the tagged/untagged ratios were calculated using the cross section models of P. Bosted [5] and E. Christy [4] within the formalism of Ref. [6]. Resolution smearing is included to better describe the measured data. We determined the number of radiation lengths that a scattered electron sees in the target (0.04 - see Fig. 1.8), and the radiated and Born cross

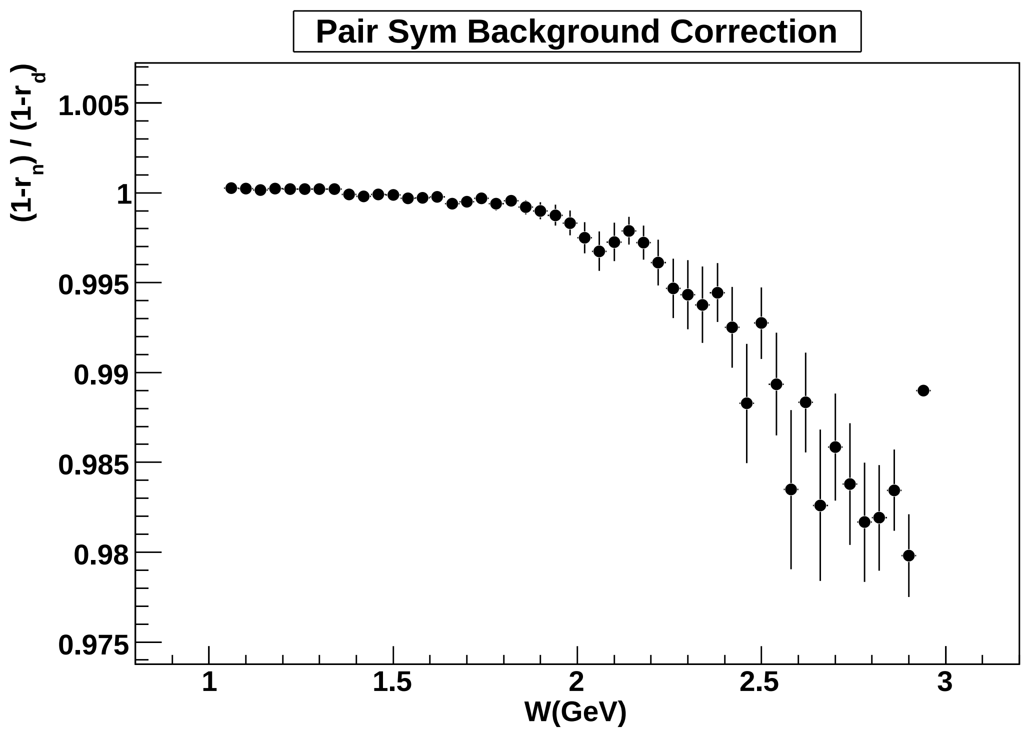

Figure 1.5: The correction to the tagged/untagged ratio due to pair symmetric background contamination.

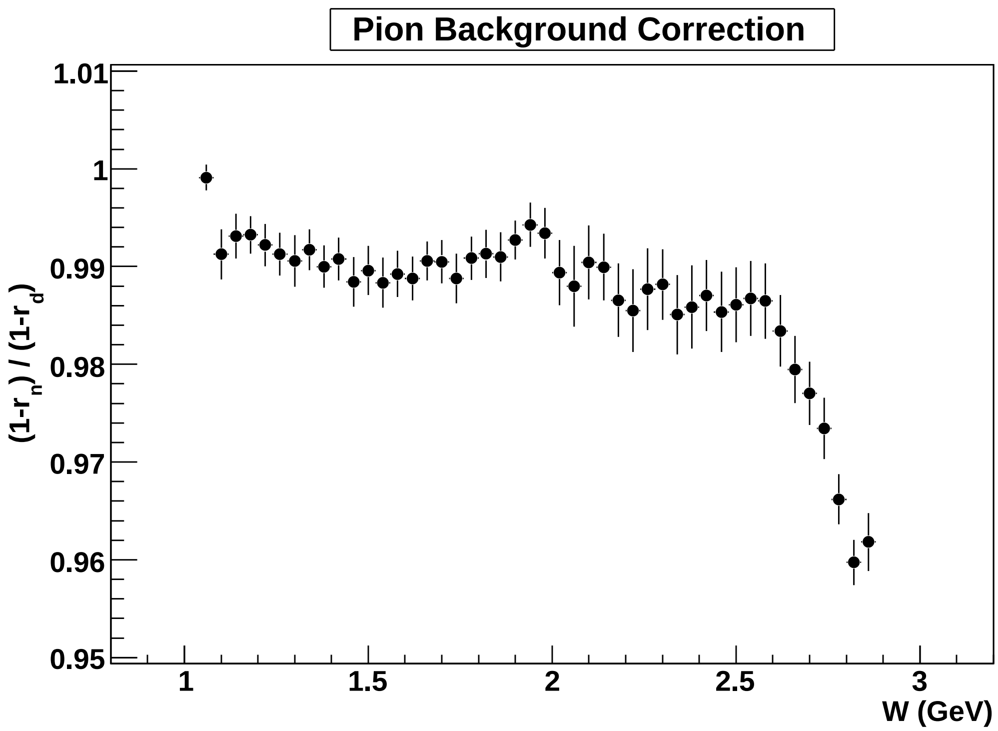

Figure 1.6: The correction to the tagged/untagged ratio due to π^- contamination. The factors r_n and r_p extracted from EG1B have both been multiplied by a factor of ten

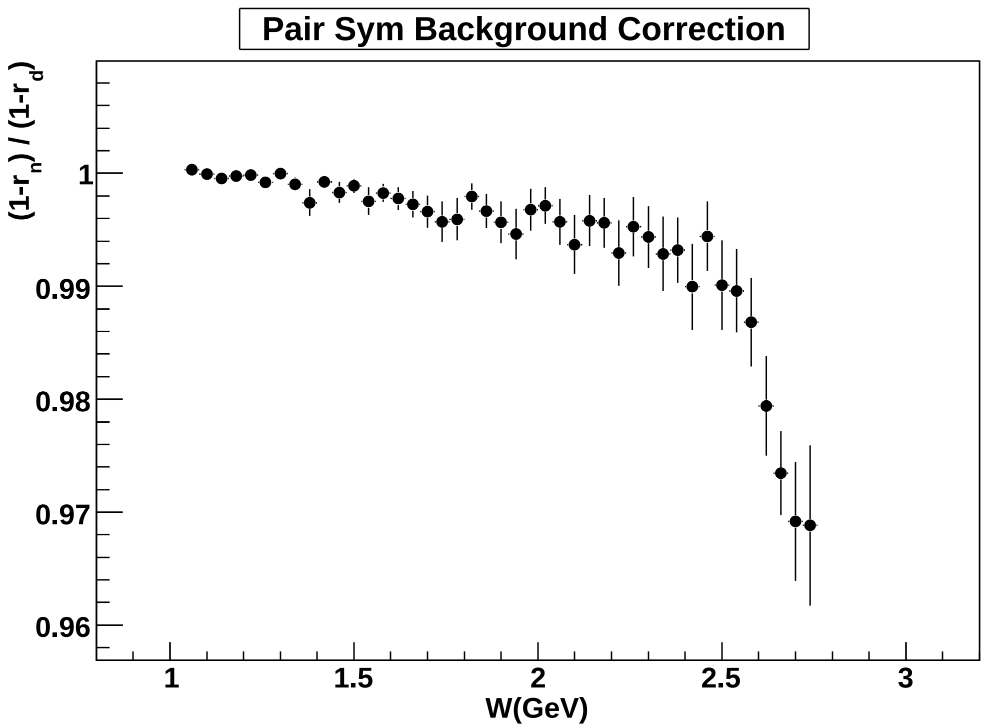

Figure 1.7: The correction to the tagged/untagged ratio due to pair symmetric background contamination. The factors r_n and r_p extracted from EG1B have both been multiplied by a factor of ten

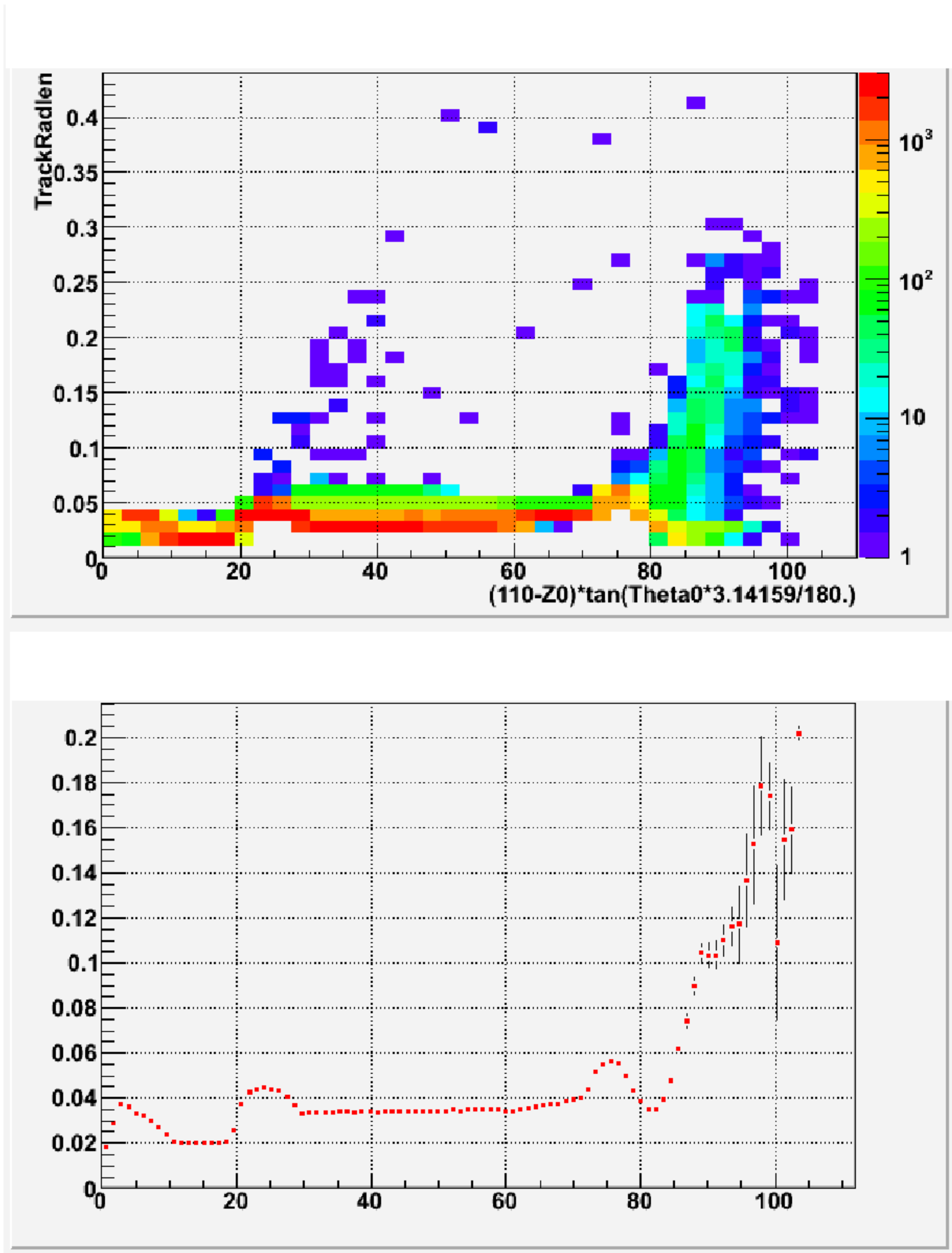

Figure 1.8: The simulated radiation length as a function of the radial position where the electron exits the cylinder defining the RTPC simulation region. The upper plot shows the distribution of radiation lengths for points around the azimuth, whereas the bottom plot shows the radiation lengths averaged for points around the azimuth. A typical forward electron travels through $\sim$0.04 radiation lengths in the target.

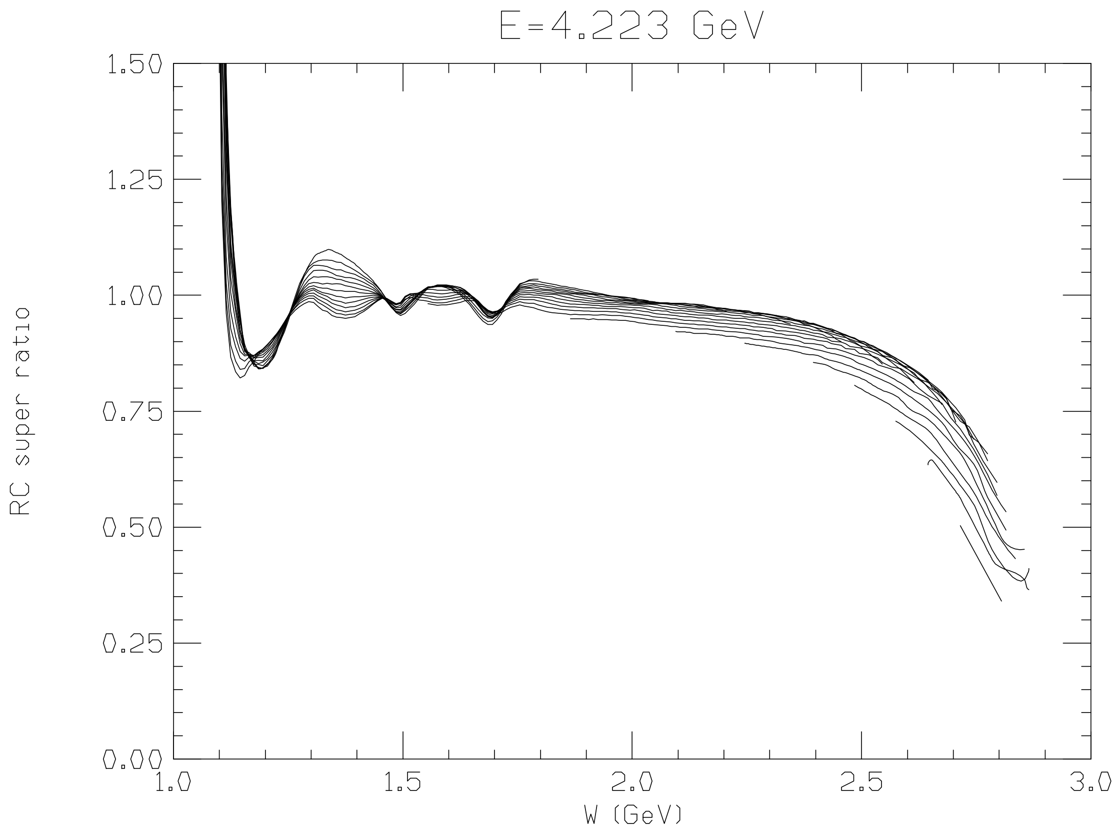

Figure 1.9: The inverse of the super ratio r_{rc} for E_{beam} = 4.223 GeV. The curves that start at higher W correspond to lowest Q^2.

sections were generated in the same bins of W and Q^2 that we bin our tagged/untagged ratio. The unpolarized cross section models also provide us the fraction of $\sigma_r^{n,d}$ coming from the elastic tail in a particular bin. We took care to avoid regions where this fraction was greater than 10%. The radiative correction is expressed as a super ratio to minimize systematic errors. Hence, we can apply a multiplicative correction to the tagged/untagged measurement:

$$r_{rc} = \frac{\sigma^n_{Born}/\sigma^n_r}{\sigma^d_{Born}/\sigma^d_r} \tag{1.12}$$

A sample of the super ratio correction (1/r_{rc}) is plotted in Figs. 1.9 and 1.10 for the 4 and 5 GeV beam energies. The different curves cover different Q^2 bins. No radiative corrections are applied to our data below $W = 1.1$ GeV because of the difficulty in getting resolution smearing to work correctly for the neutron elastic peak.

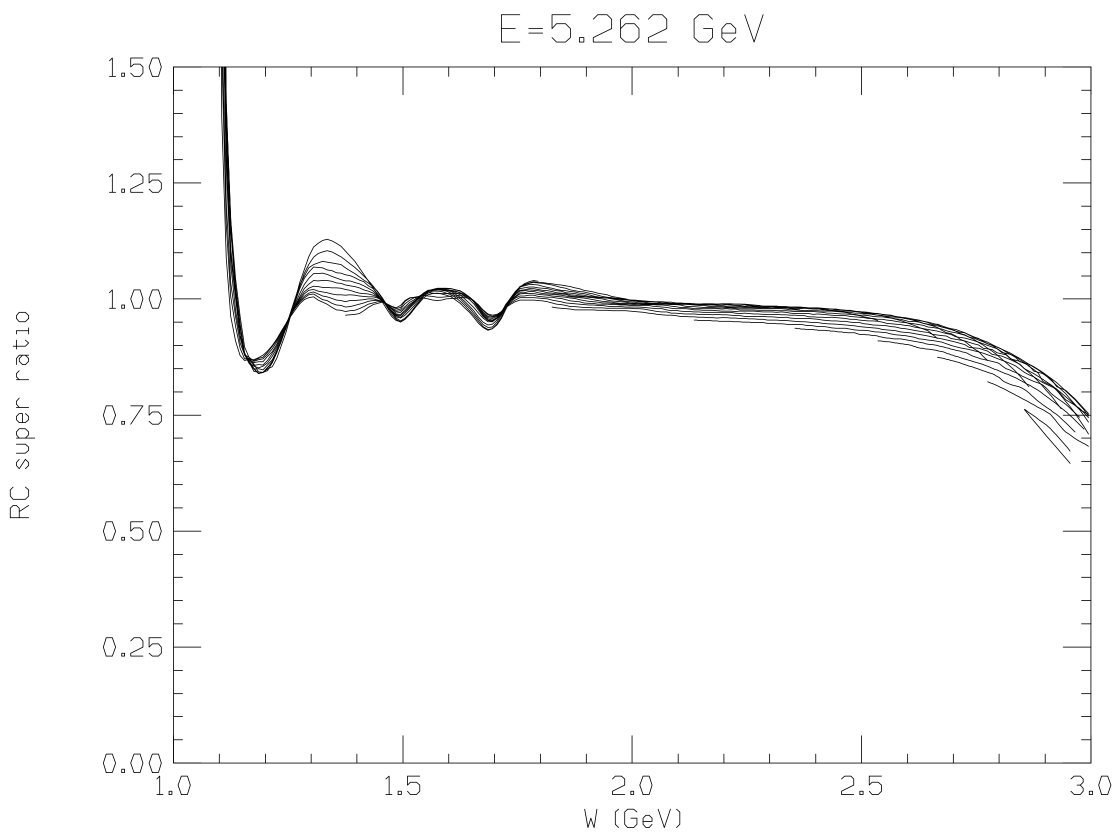

Figure 1.10: The inverse of the super ratio r_{rc} for $E_{beam} = 5.262$ GeV. The curves that start at higher W correspond to lowest Q^2.

1.2.5 Structure Function Ratio Extraction

A sample of the untagged and tagged distributions can be seen in Fig. 1.11. Clearly the calculation of the proper invariant mass of the neutron, W^*, sharpens the quasi-elastic peak and the resonances begin to take shape as we would expect from inclusive scattering on a free nucleon. Once we have accumulated the corrected tagged/untagged counts in bins of W and Q^2 (see Fig. 1.12 for our kinematic coverage), we can go on to our final step of extracting structure function ratios.

We converted the tagged/untagged ratio, R_{corr}, into a ratio of structure functions by applying all of the multiplicative correction factors. Thus,

$$\frac{F_2^n}{F_2^d} = (R_{corr})(C_{e^+})(C_\pi)(r_{rc})(n) \tag{1.13}$$

in which n is the RTPC efficiency correction found in Sec. 1.2.2, C_{e^+} and C_π are the pion and pair symmetric contamination corrections found by Eq. 1.11, r_{rc} is the radiative correction super ratio found in Eq. 1.12. This assumes that the R structure function is identical for the neutron and the deuteron. Because this quantity is not precisely measured, this assumption feeds into the systematic errors

Using the well-measured and parameterized deuteron to proton structure function ratio, F_2^d/F_2^p, we obtain

$$\frac{F_2^n}{F_2^p} = \left(\frac{F_2^n}{F_2^d}\right)\left(\frac{F_2^d}{F_2^p}\right)_{\text{model}}. \tag{1.14}$$

Multiplying Eq. 1.14 by $F^p_{2(\text{model})}$ provides an extraction of F_2^n. Also we can further extract a measurement of d/u, once we have the nucleon structure function ratio, by applying Eq. **??**.

Since W^* is always less than W there is a steep fall off to the tagged/untagged ratio at the edge of the experiment's W acceptance. This is an unavoidable result of the kinematics and can be removed with a simple Q^2-dependent cut on the maximum invariant mass. This cut has been made on all of the plots using the Ratio Method.

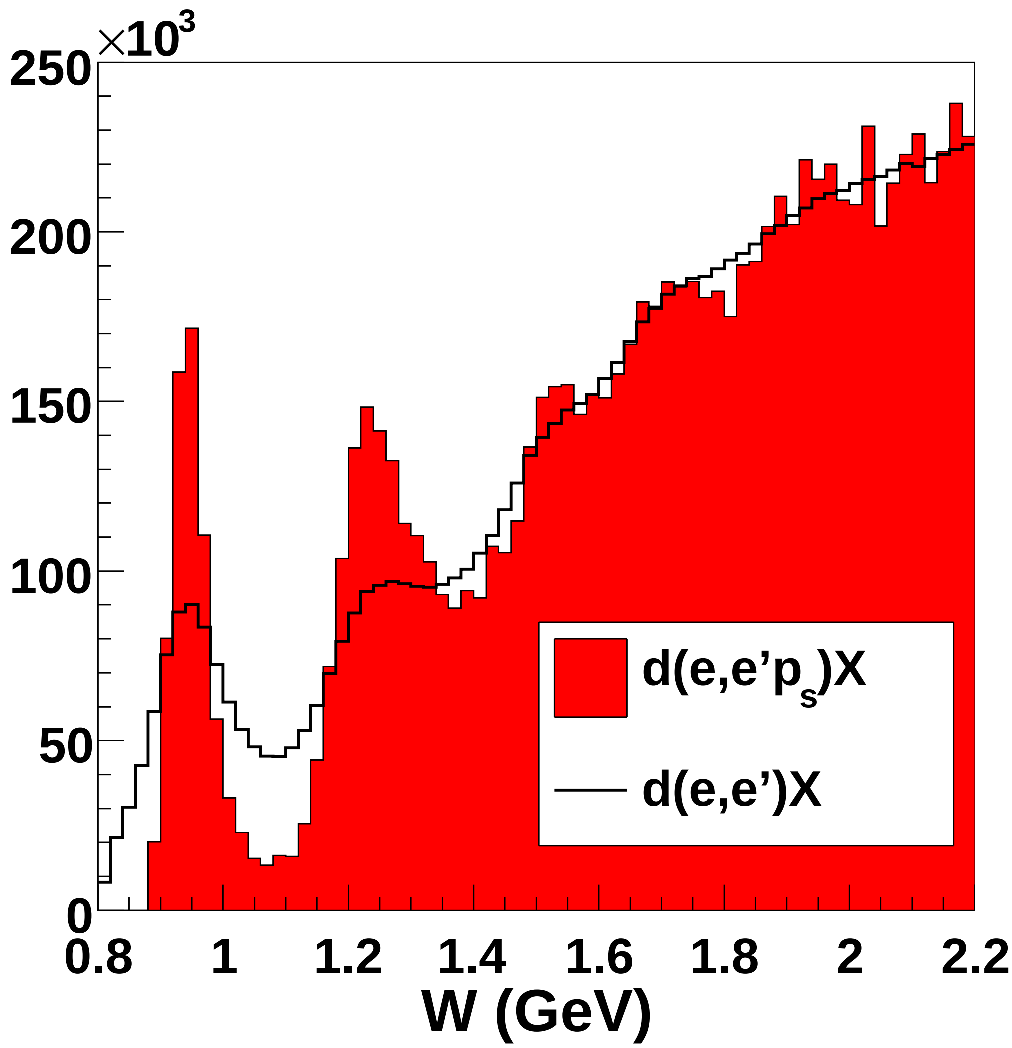

Figure 1.11: Inclusive scattering on deuterium (black line) representing our untagged data sample as a function of W and the corresponding tagged sample as a function of the corrected mass W^*. The data are normalized so that the area under the curves is equal. $E_{beam} = 4.223$ GeV

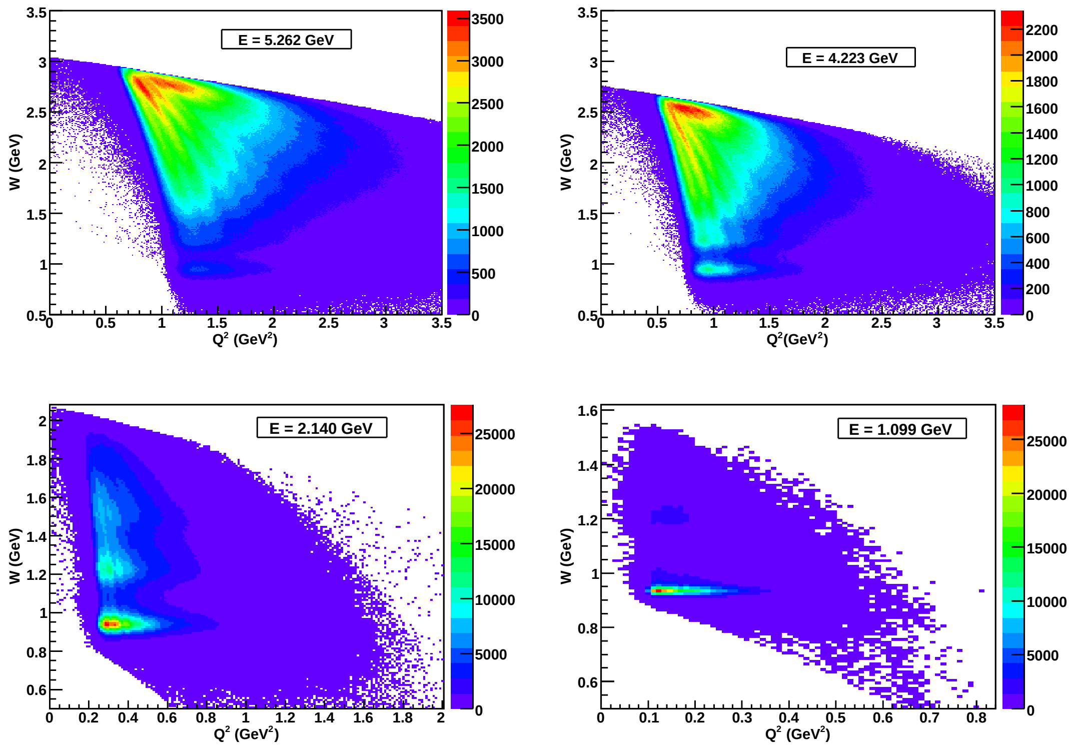

Figure 1.12: The kinematic coverage in invariant mass and momentum transfer for each of the four BoNuS beam energies.

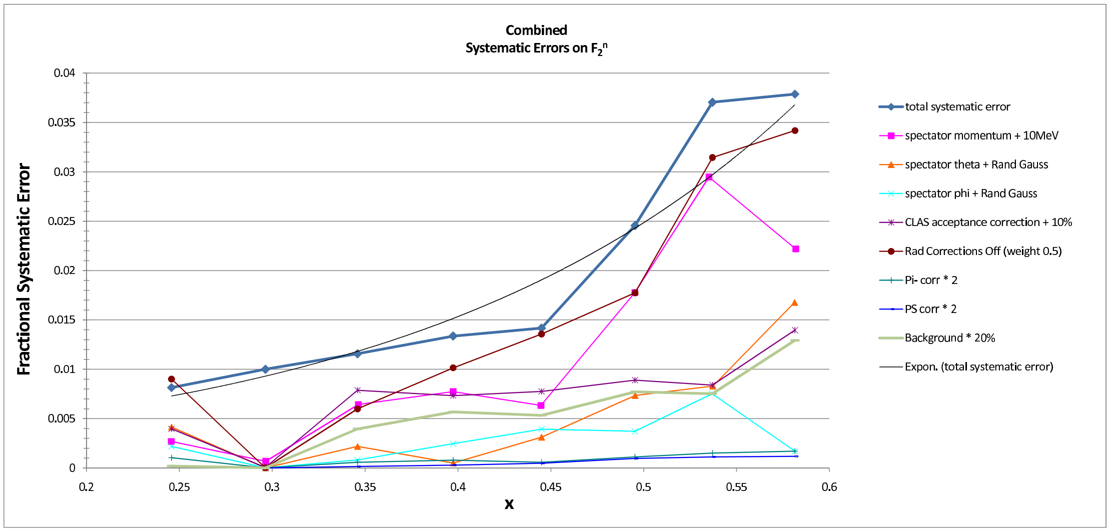

Figure 1.13: Fractional systematic errors as a function of x for the deep-inelastic F_2^n/F_2^p results. The total rises from about 1% at low x to about 4% at high x. These errors are obtained by changing various corrections, redoing the full analysis, and looking at the difference between the new values as compared to the nominal ones.

1.2.6 Error Estimation

The statistical error on the acceptance corrected counts is simply $\sqrt{\sum_{i=1}^{N} \frac{1}{\epsilon_i^2(W,Q^2)}}$ for each summation in the numerator and denominator, properly propagated through to give the total statistical error on R_{corr} in Eq. 1.1. The systematic error on each of the multipliers in Eq. 1.13 is given in Table 1.1.

The experimental technique used in this analysis has the advantage of canceling out some typical sources of systematic errors. These errors include, but are not limited to, the EC ID cut, the trigger efficiency, and CC efficiency. Presumably, the normalization error of 5% could be reduced at a later date upon the successful completion of the RTPC efficiency Monte Carlo simulations.

For the F_2^n/F_2^p data versus x, we have redone the full analysis (including the overall normalization at $x = 0.3$) with various changes in our correction factors in order to estimate the overall systematic errors. Plotted in Fig. 1.13 are the results of this study as a function of x. The pink squares correspond to increasing the observed spectator momentum by 10 MeV/c.

Correction Factor	**Estimated Systematic Error (%)**	**Explanation**
FSI	5.0	The uncertainty coming from the effect of final state interactions at spectator kinematics. [15]
Target Fragmentation	1.0	The uncertainty coming from the effect of target fragmentation at spectator kinematics. [13]
Off-Shell	1.0	The uncertainty coming from the effect of nucleon off-shellness at spectator kinematics. [16]
C_{e^+}	1.0	Assuming our pair symmetric background contamination is less than 10 times than the amount in the EG1B experiment, Fig. 1.7 shows that amount of correction to the ratio is less than 1%.
C_π	1.0	Same argument as above, only reference Fig. 1.6.
r_{rc}	2.0	Each value of $\sigma_b(E, W, Q^2)$ and $\sigma_r(E, W, Q^2)$ for the neutron and the deuteron has an uncertainty of 1% leading to a 2% error on the ratio.
n	5.0	The approximate deviation from a flat normalization as seen in Fig. 1.3.
F_2^d/F_2^p	4.2	The error quoted in [5] and [4] on the fits to the structure functions is 3% which leads to an error of 4.2% on our ratio.
Total Error	8.7	After adding all these errors in quadrature.

Table 1.1: The total systematic error on the ratio F_2^n/F_2^p. Each error is quoted in percentage of the ratio and the estimation explanation is found in the last column.

This corresponds roughly to our momentum resolution, and an incorrect momentum implies an incorrect correction from W to W^*. The plot shows the percentage difference between the extracted F_2^n/F_2^p in this case, compared to the nominal values. The orange triangles correspond to changing each observed spectator angle θ_{pq} by a random Gaussian-distributed offset with $\sigma = 5°$. The blue X's correspond to a similar modification in the azimuthal angle ϕ. The purple stars correspond to adding 10% to the CLAS acceptance values $\epsilon(W, Q^2)$; this is an overestimate, since the average deviations between the model and data for the deuteron is only 3%. The red circles correspond to cutting the radiative corrections in half. The green +'s correspond to multiplying the pion correction by a factor of two. The blue dots correspond to multiplying the pair-symmetric background by a factor of two. The olive bars correspond to increasing the subtracted background by 20%. The blue diamonds correspond to all of these effects added in quadrature. The solid black line is an exponential fit to the total of the form $0.0022 \exp 4.8231x$. Because of the normalization condition, the point near $x = 0.3$ remains close to zero in all cases. The total error near $x = 0.3$ is an interpolation from the values on either side so that a smooth fit to these data is possible. The rise in uncertainty at high x is expected because here the nuclear corrections from the spectator tagging are large. This error is dominated by uncertainties in the spectator momentum and radiative corrections (the later of which depends on the accuracy of the models for the neutron and the deuteron in this region.

1.2.7 F_2^n/F_2^d, F_2^n/F_2^p and F_2^n

This section contains the graphs of the results of the extraction of F_2^n/F_2^d, F_2^n/F_2^p, F_2^n from the measured and corrected tagged/untagged ratio following the prescription of Eq. 1.13. The group of graphs from Fig. 1.14 through 1.31 contain the structure function ratios and F_2^n as a function of W^* and x^*, for bins in Q^2 where there were enough counts to be statistically significant. The parameterization of Refs. [5] and [4] (a fit to previous data that all have nuclear model uncertainties) is shown as well.

The parameterization and the data are in rough agreement, with differences expected because these data are the first direct measurements of F_2^n without nuclear model-dependence.

The slight differences in the observed and model locations of the Δ resonance could be caused by: 1) the model being quoted at a fixed average Q^2, whereas the average Q^2 in a bin varying slightly across the spectrum; 2) the Δ riding on a steeply rising but poorly modeled backgroud that shifts the peak; and 3) a second-order effect from the interplay between tagged corrections, which sharpen the Δ peak, and a rapidly changing acceptance in this region, which, if slightly off, can shift a peak. Our systematic errors are large enough to encompass all of this.

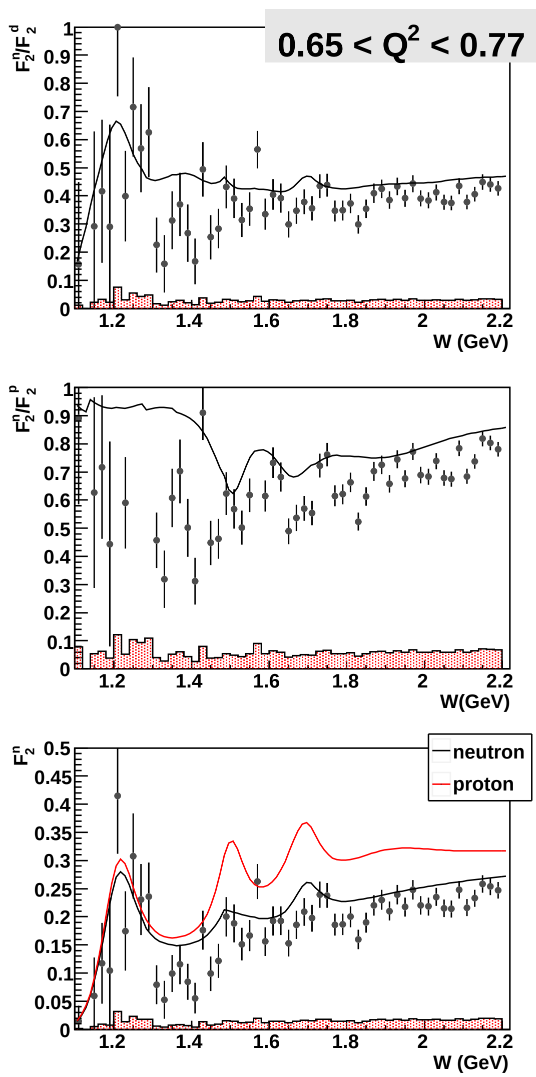

Figure 1.14: F_2^n/F_2^d, F_2^n/F_2^p, and F_2^n versus W^* and x^* at $0.65 < Q^2 < 0.77$ GeV^2, $E_{beam} =$ 4.223 GeV. The neutron and proton lines are from the phenomenological model of Refs. [5] and [4].

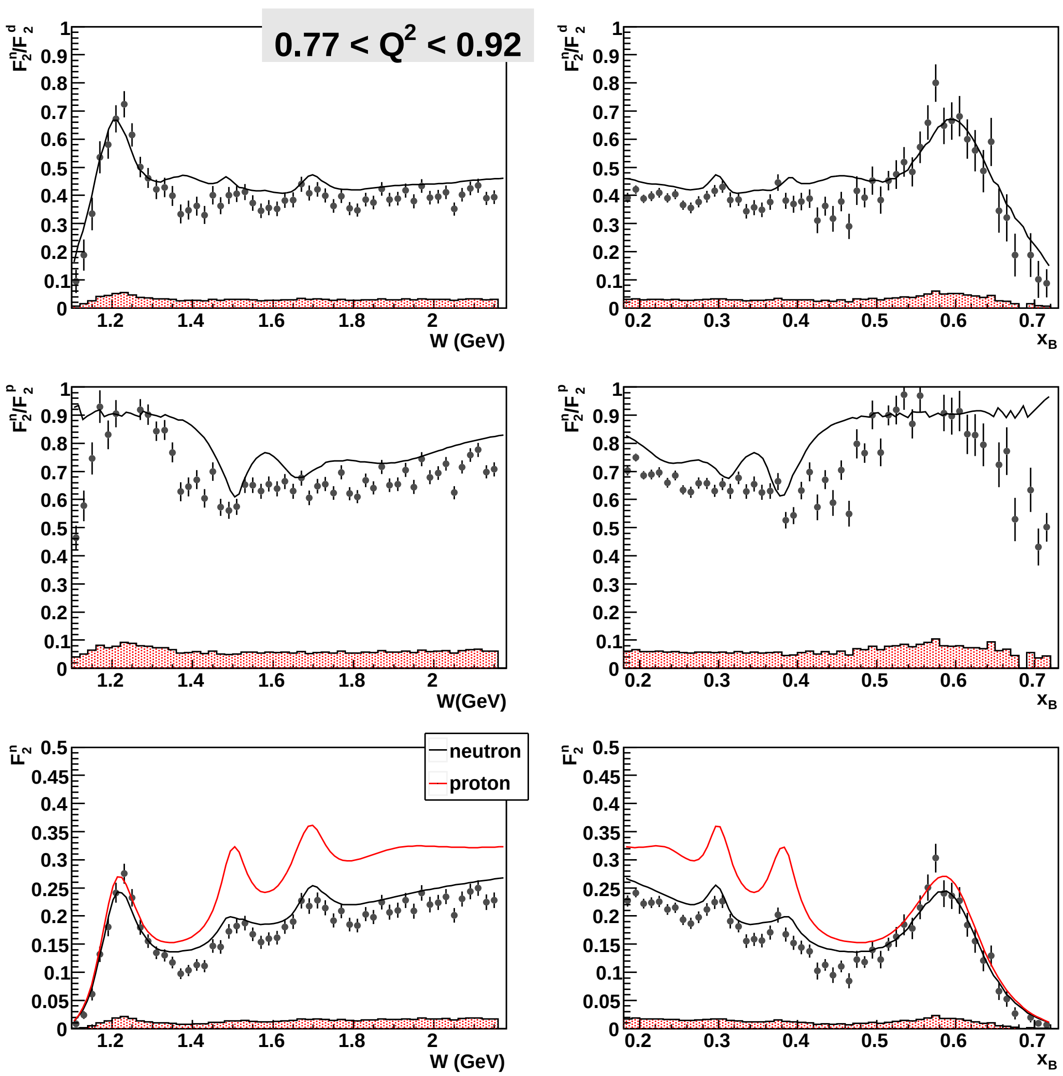

Figure 1.15: Same as Fig. 1.14 but at $0.77 < Q^2 < 0.92$ GeV^2.

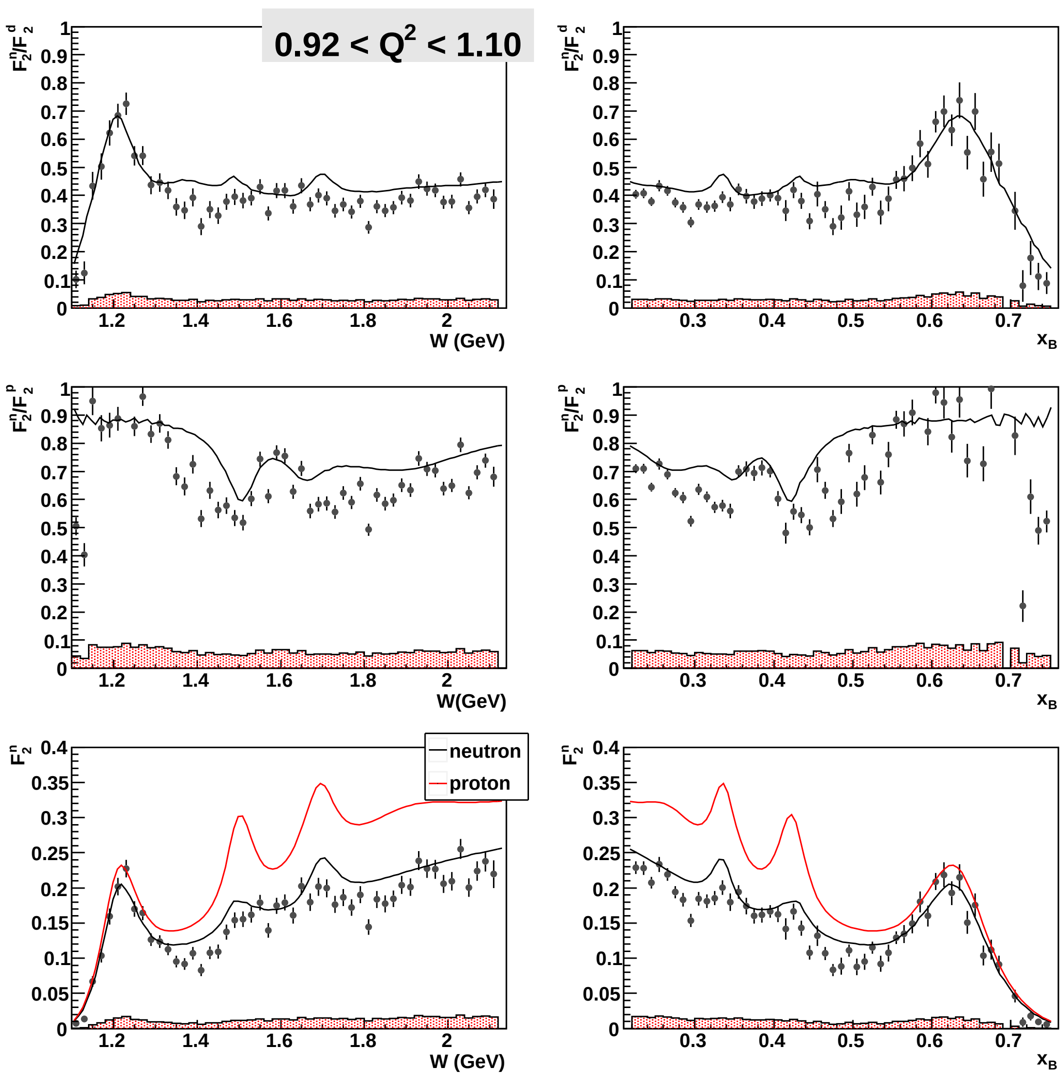

Figure 1.16: Same as Fig. 1.14 but at $0.92 < Q^2 < 1.10$ GeV^2.

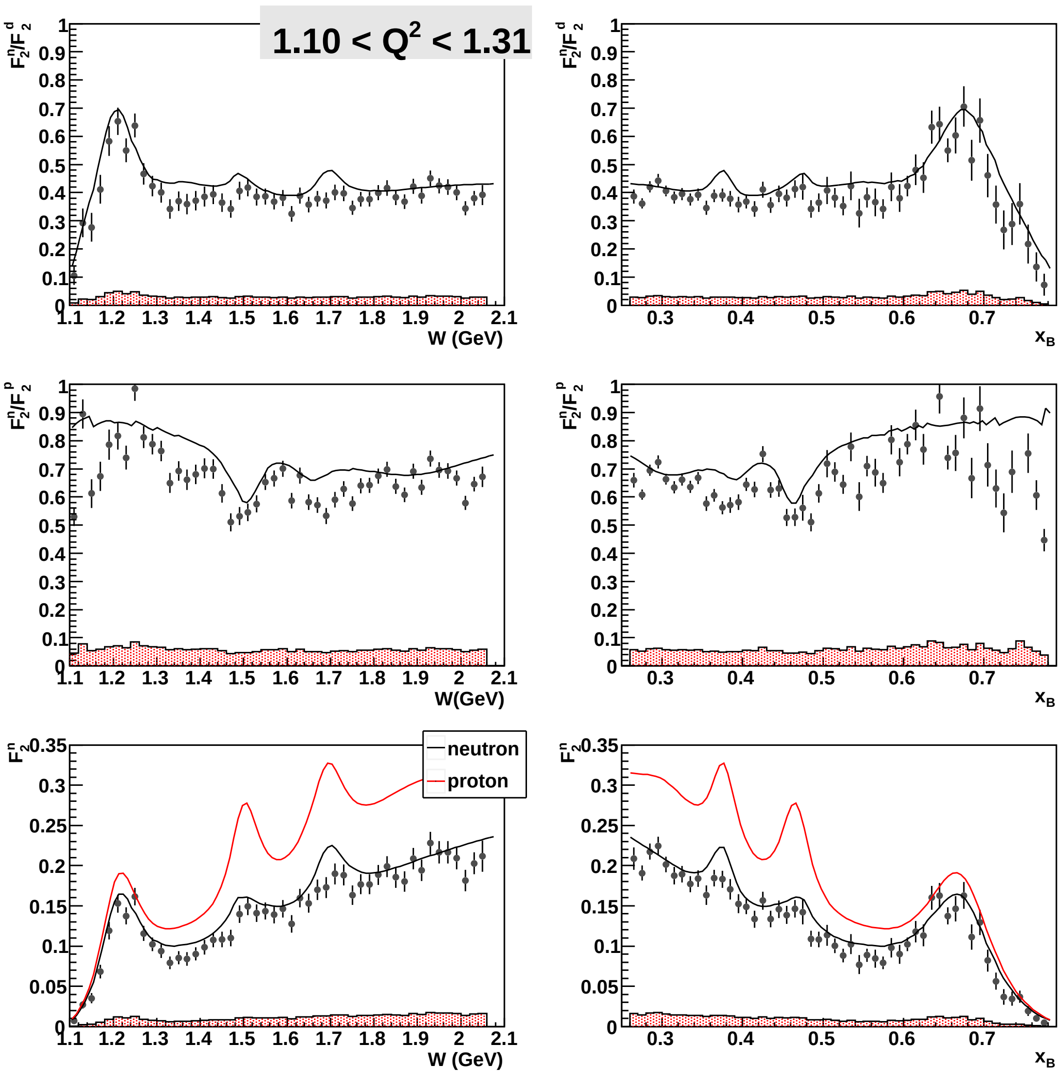

Figure 1.17: Same as Fig. 1.14 but at $1.10 < Q^2 < 1.31$ GeV^2.

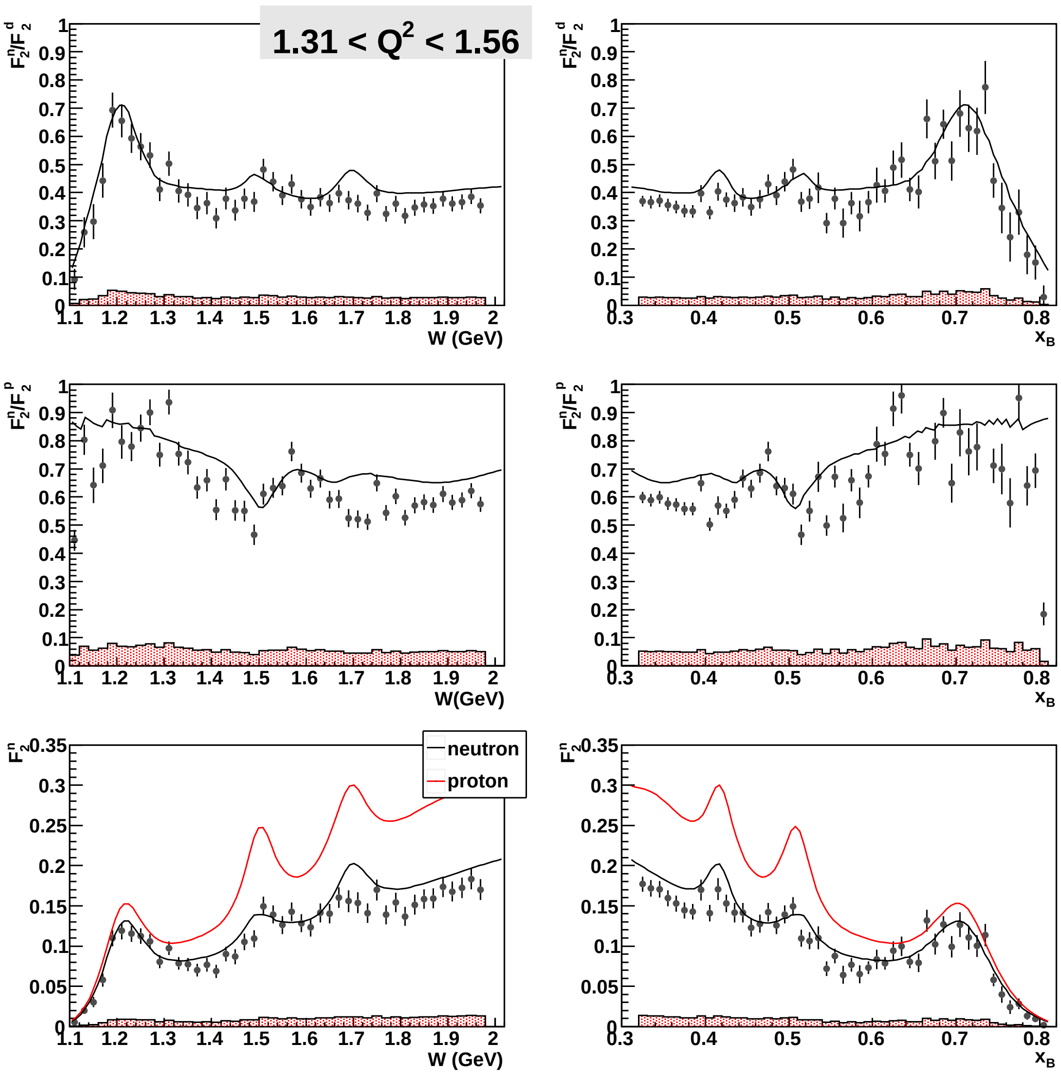

Figure 1.18: Same as Fig. 1.14 but at $1.31 < Q^2 < 1.56$ GeV^2.

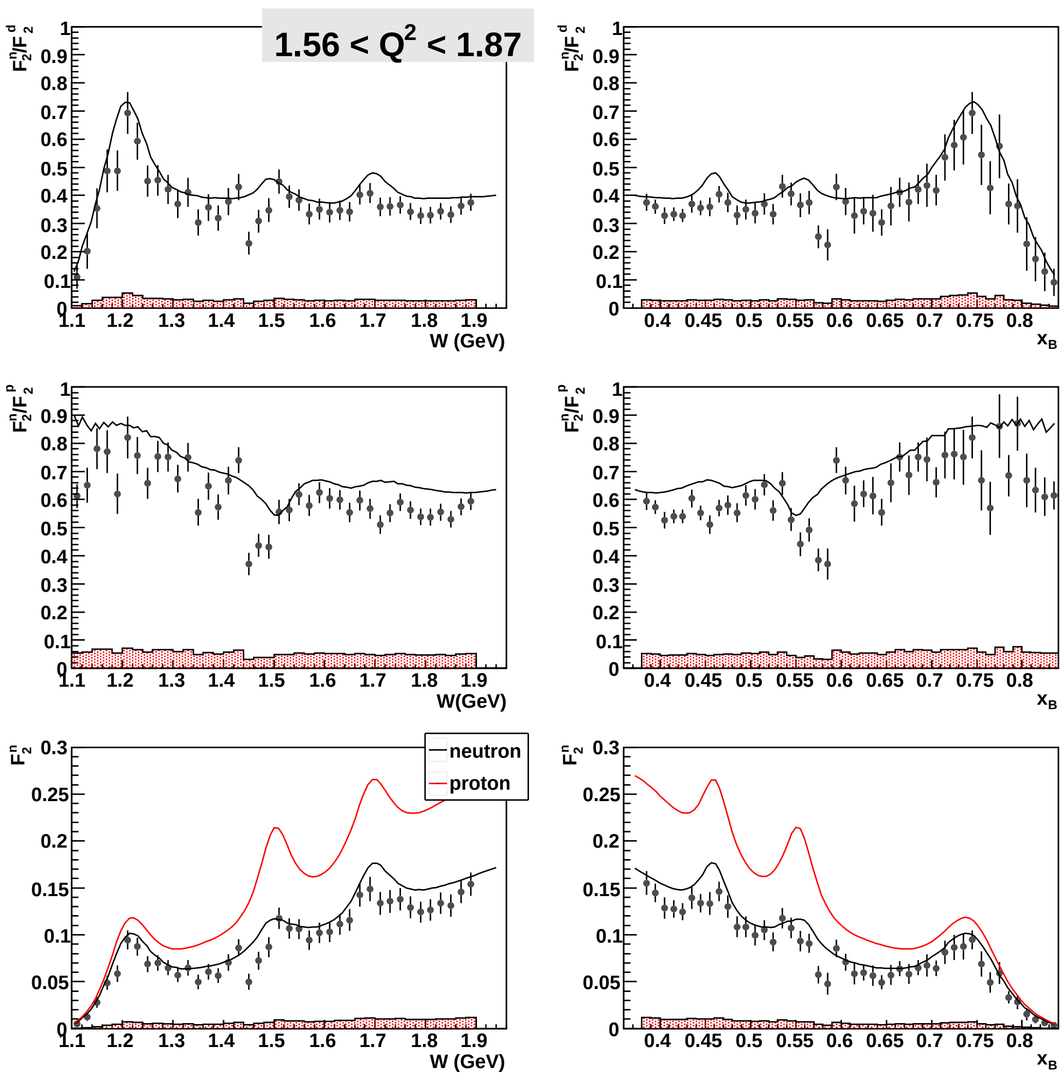

Figure 1.19: Same as Fig. 1.14 but at $1.56 < Q^2 < 1.87$ GeV^2.

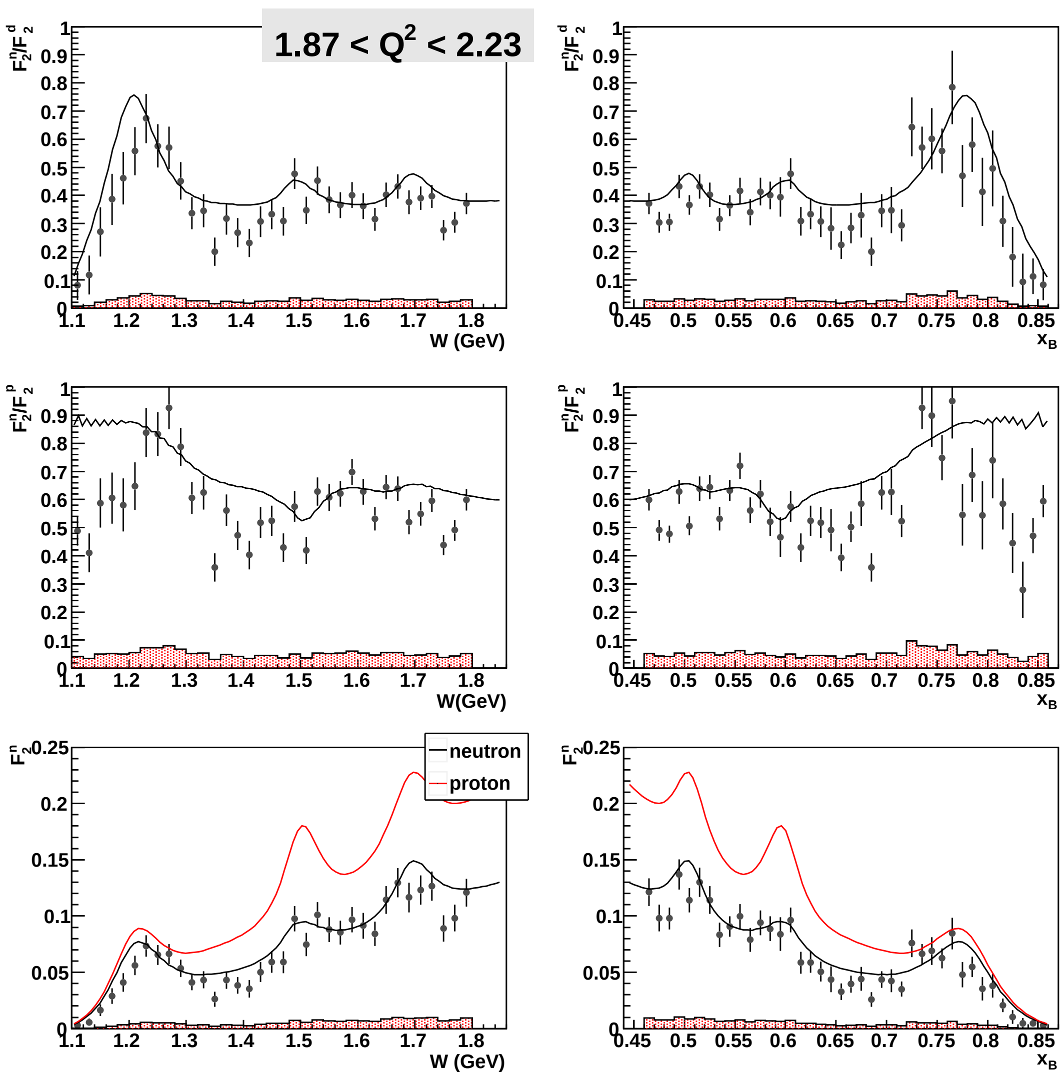

Figure 1.20: Same as Fig. 1.14 but at $1.87 < Q^2 < 2.23$ GeV^2.

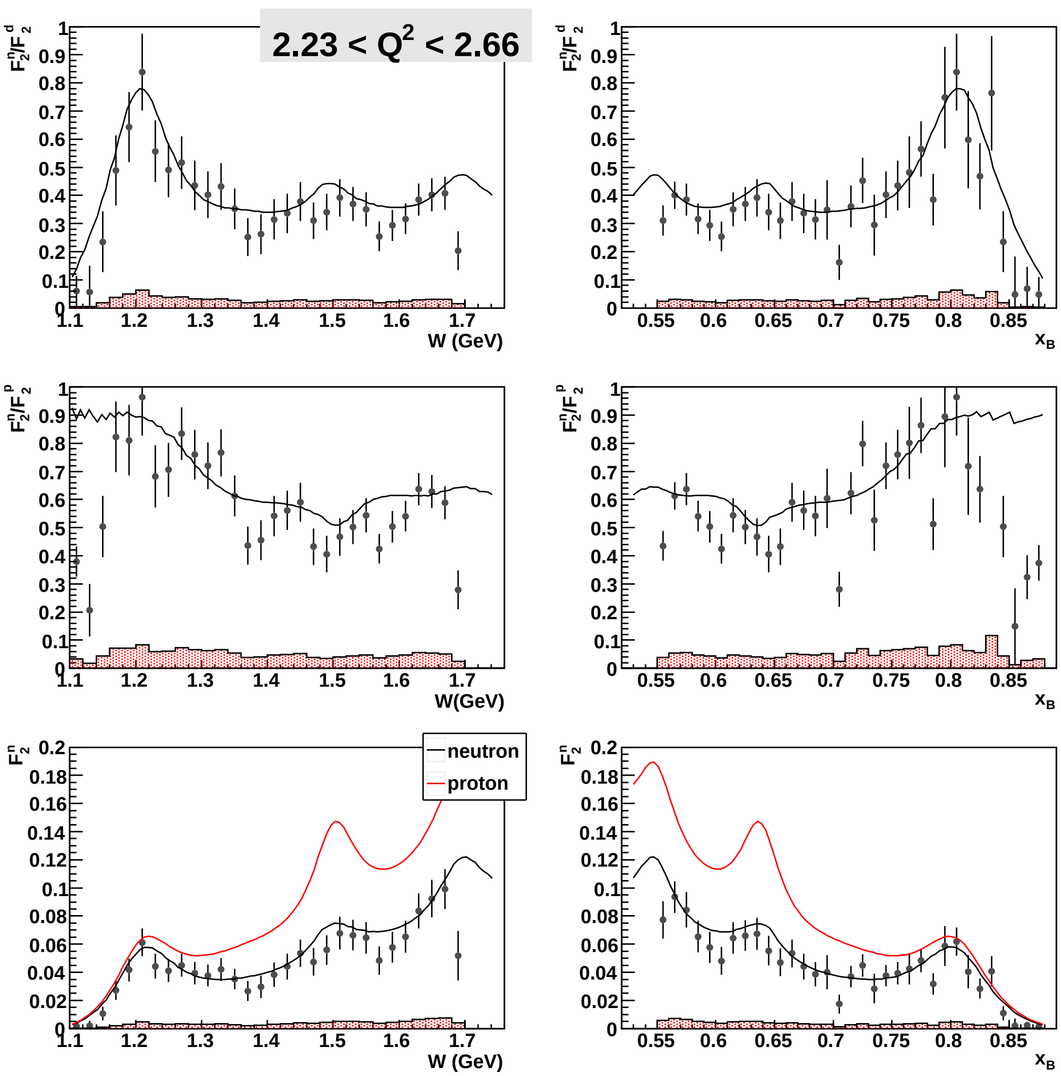

Figure 1.21: Same as Fig. 1.14 but at $2.23 < Q^2 < 2.66$ GeV^2.

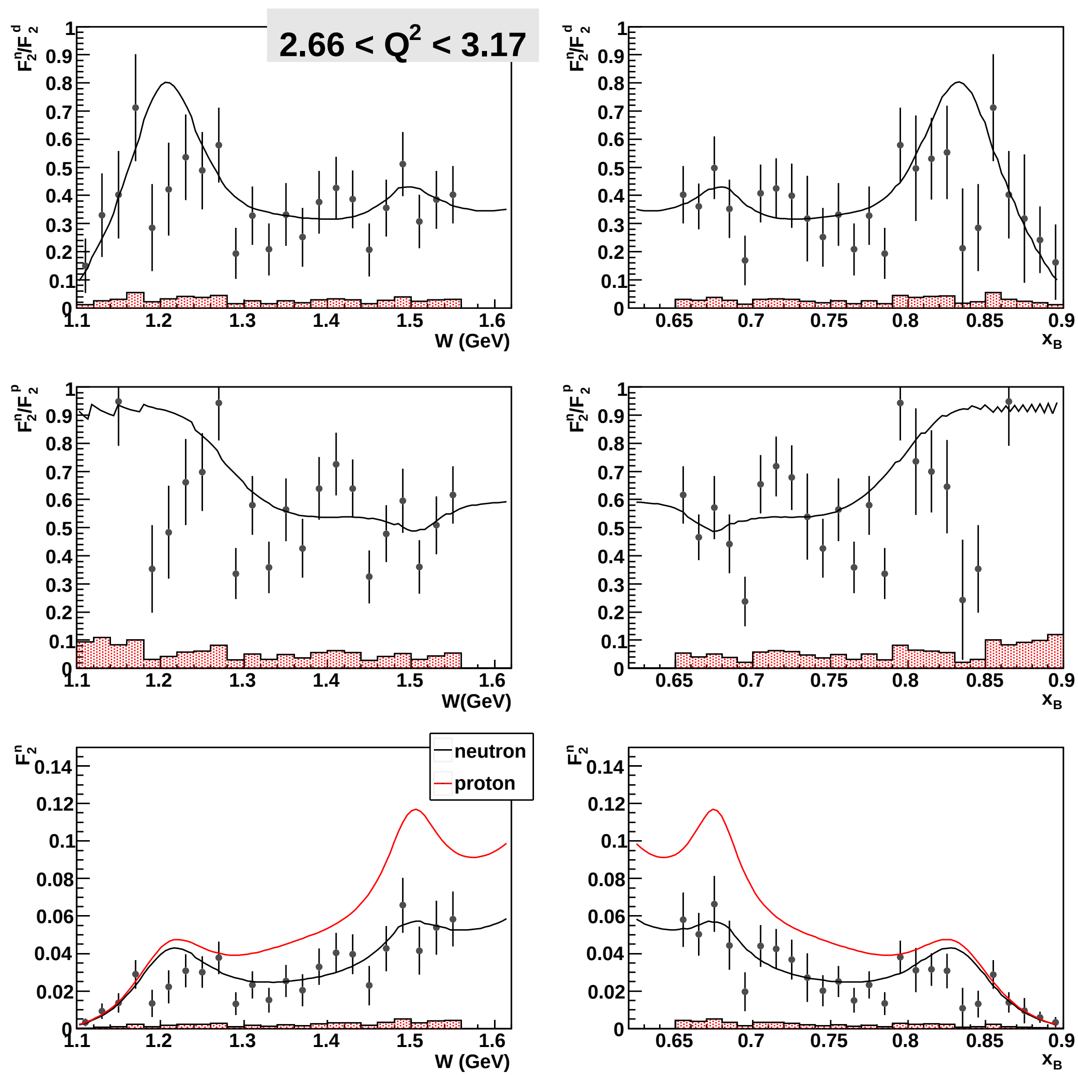

Figure 1.22: Same as Fig. 1.14 but at $2.66 < Q^2 < 3.17$ GeV^2.

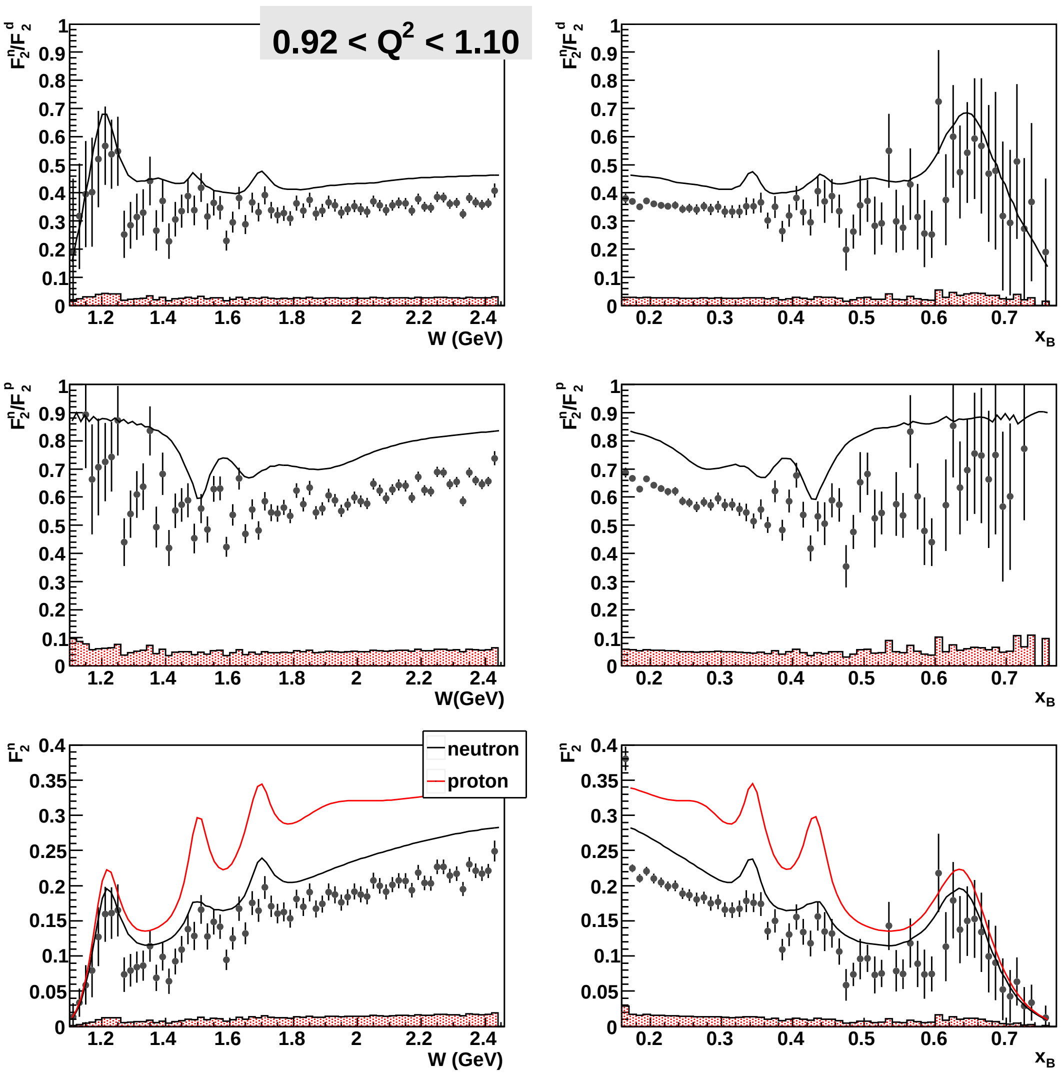

Figure 1.23: F_2^n/F_2^d, F_2^n/F_2^p, and F_2^n versus W^* and x^* at $0.92 < Q^2 < 1.10$ GeV^2, $E_{beam} =$ 5.262 GeV. The neutron and proton lines are from the phenomenological model of Refs. [5] and [4].

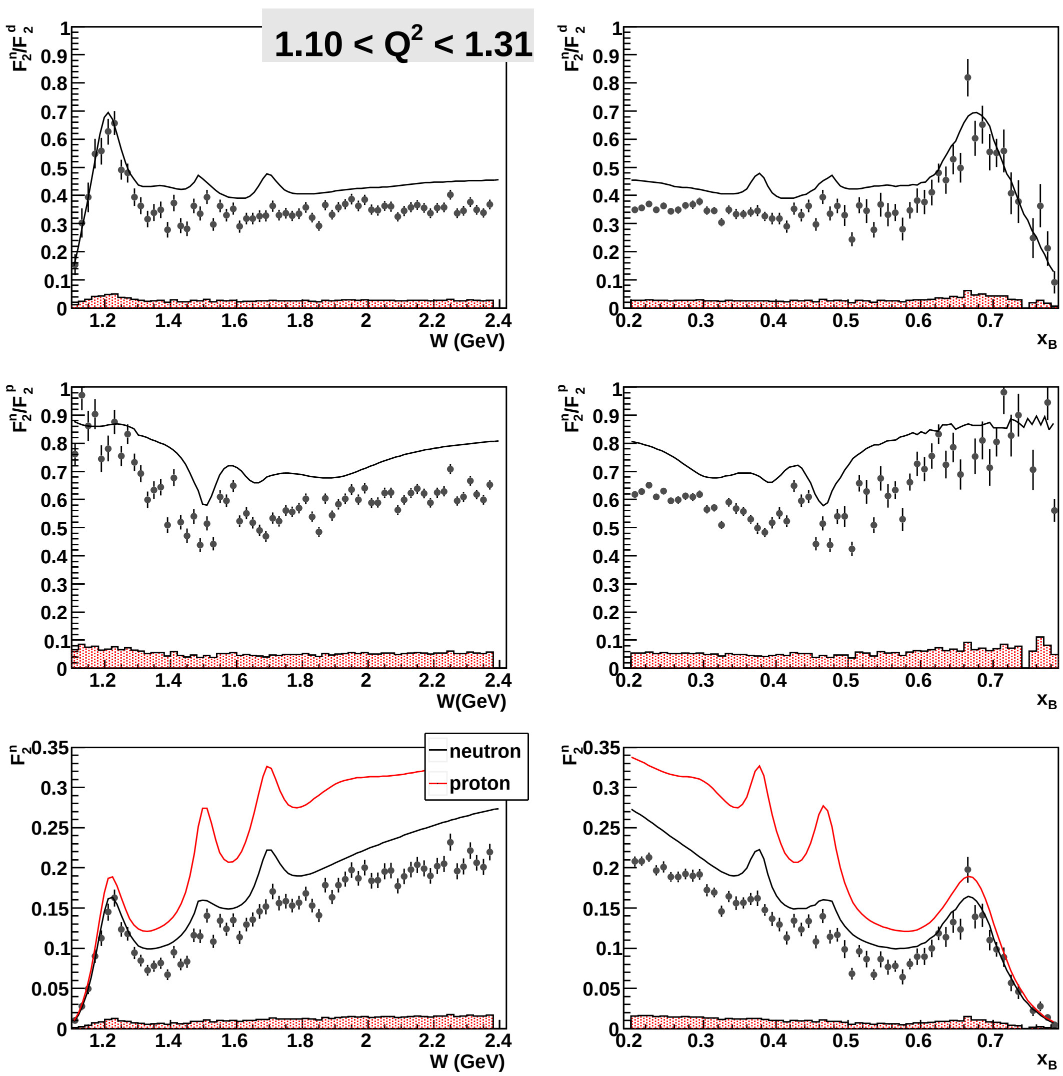

Figure 1.24: Same as Fig. 1.23 but at $1.10 < Q^2 < 1.31$ GeV^2.

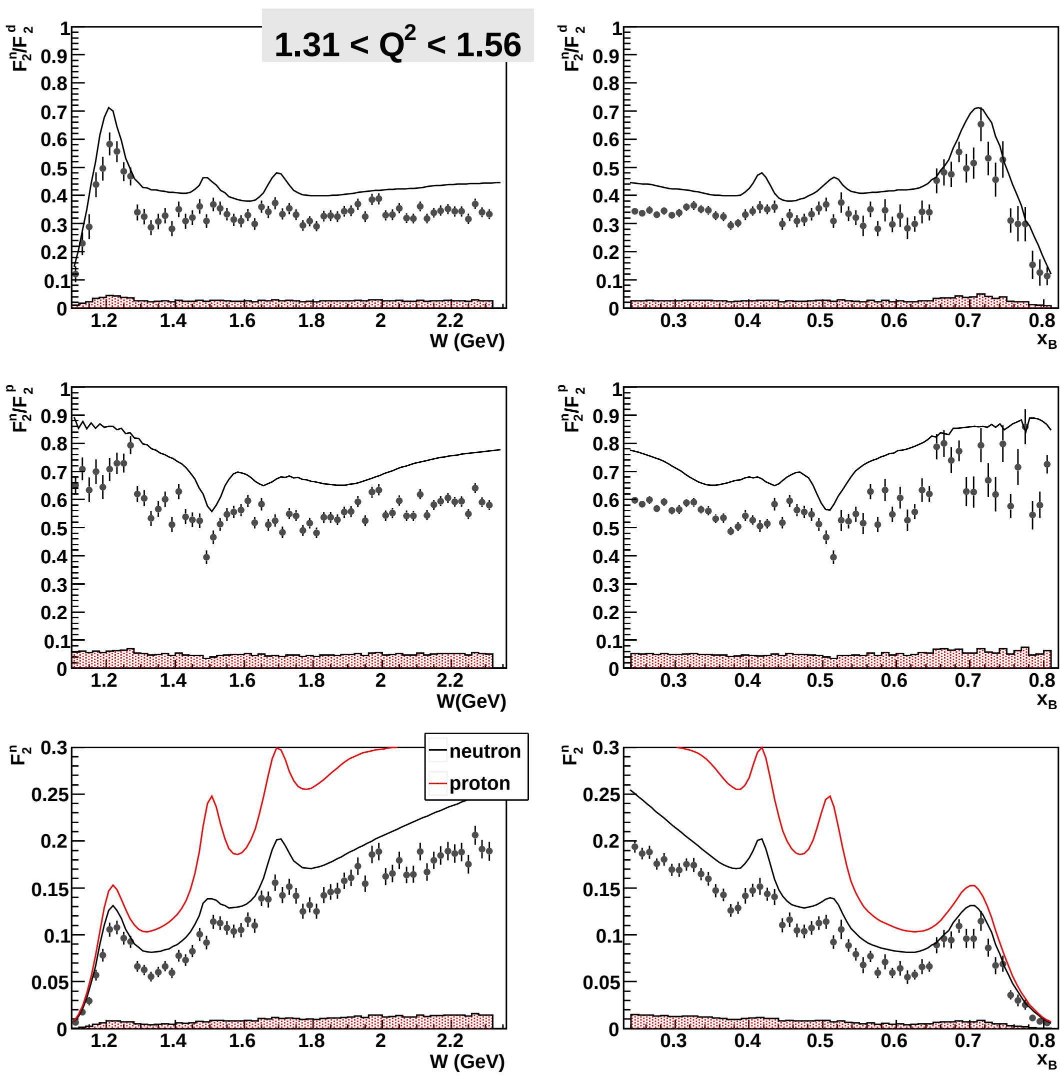

Figure 1.25: Same as Fig. 1.23 but at $1.31 < Q^2 < 1.56$ GeV^2.

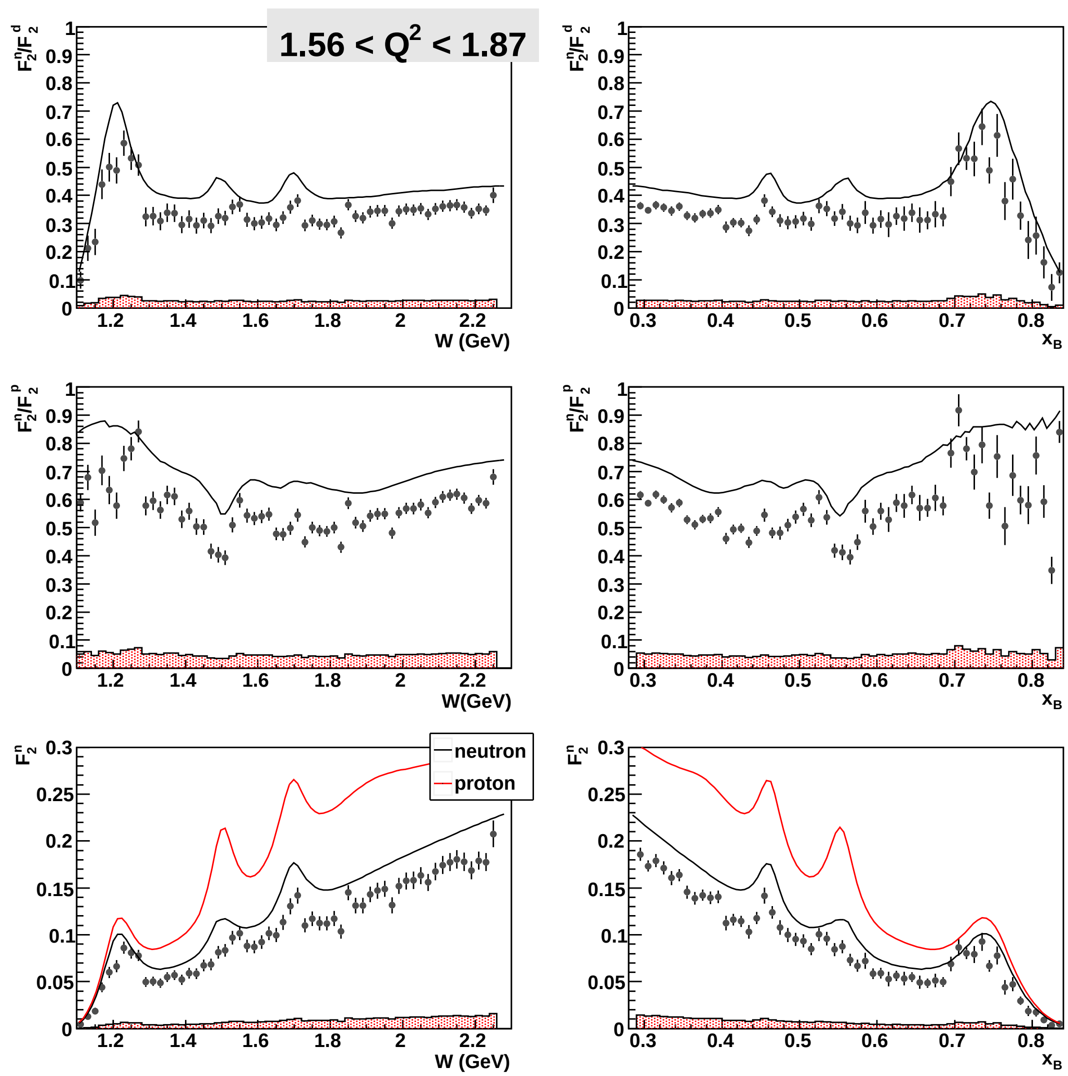

Figure 1.26: Same as Fig. 1.23 but at $1.56 < Q^2 < 1.87$ GeV^2.

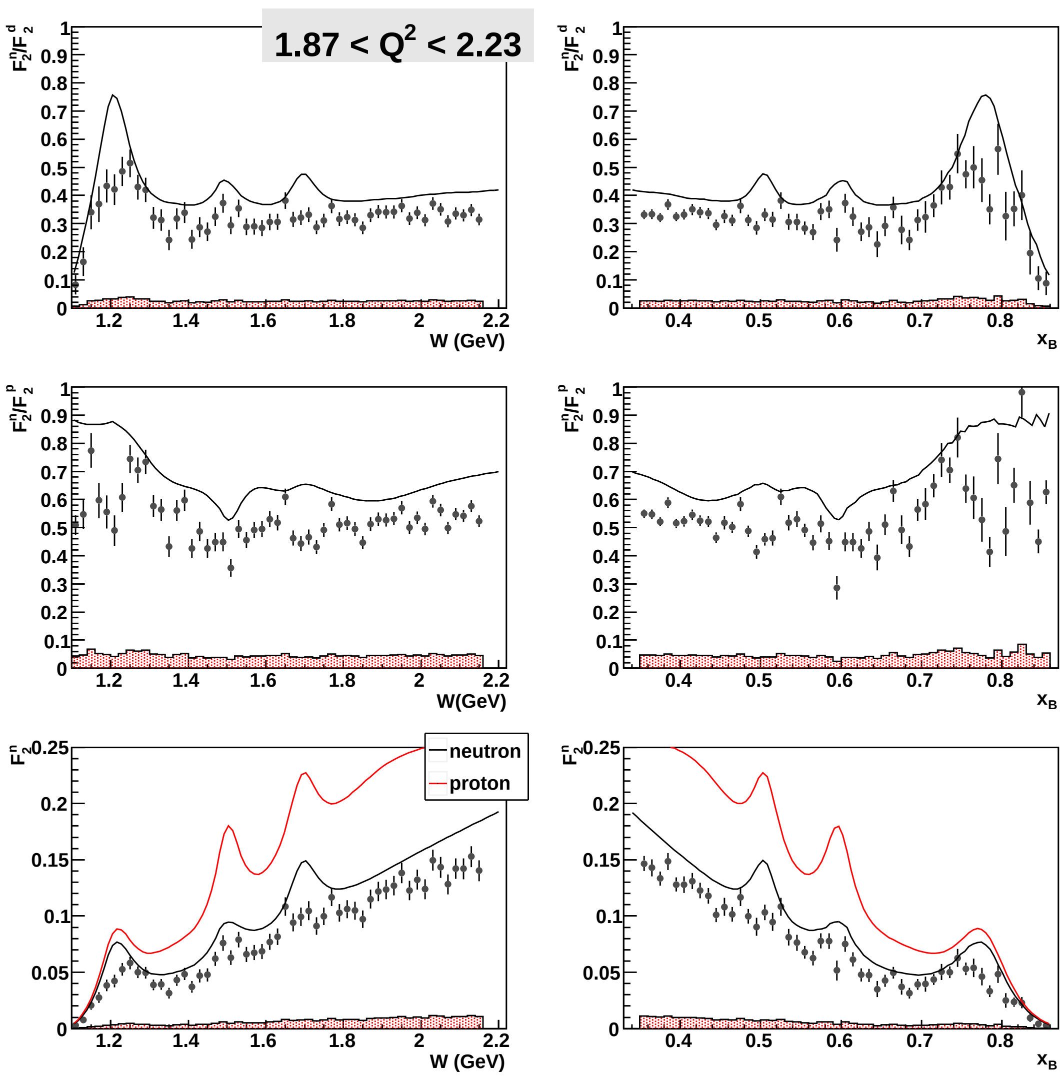

Figure 1.27: Same as Fig. 1.23 but at $1.87 < Q^2 < 2.23$ GeV^2.

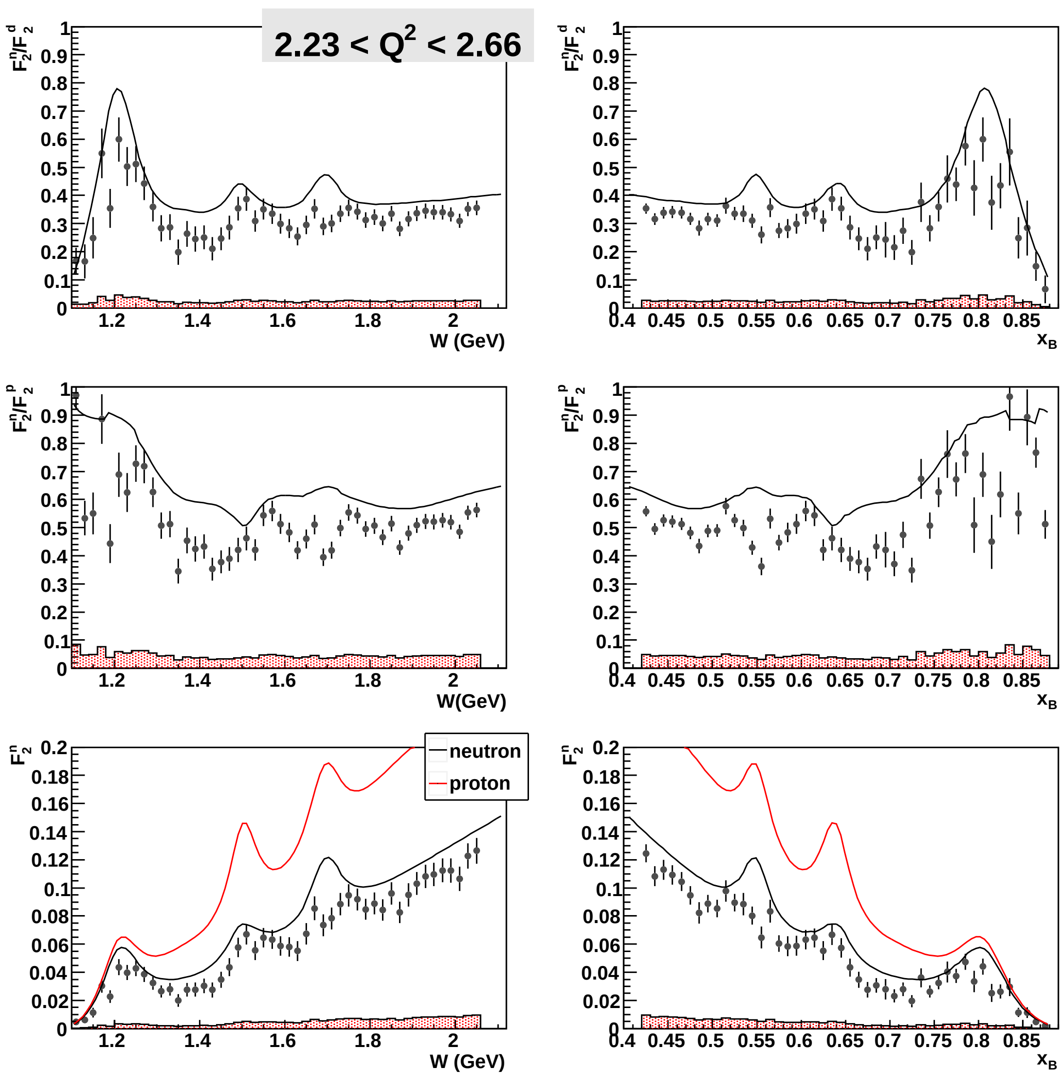

Figure 1.28: Same as Fig. 1.23 but at $2.23 < Q^2 < 2.66$ GeV^2.

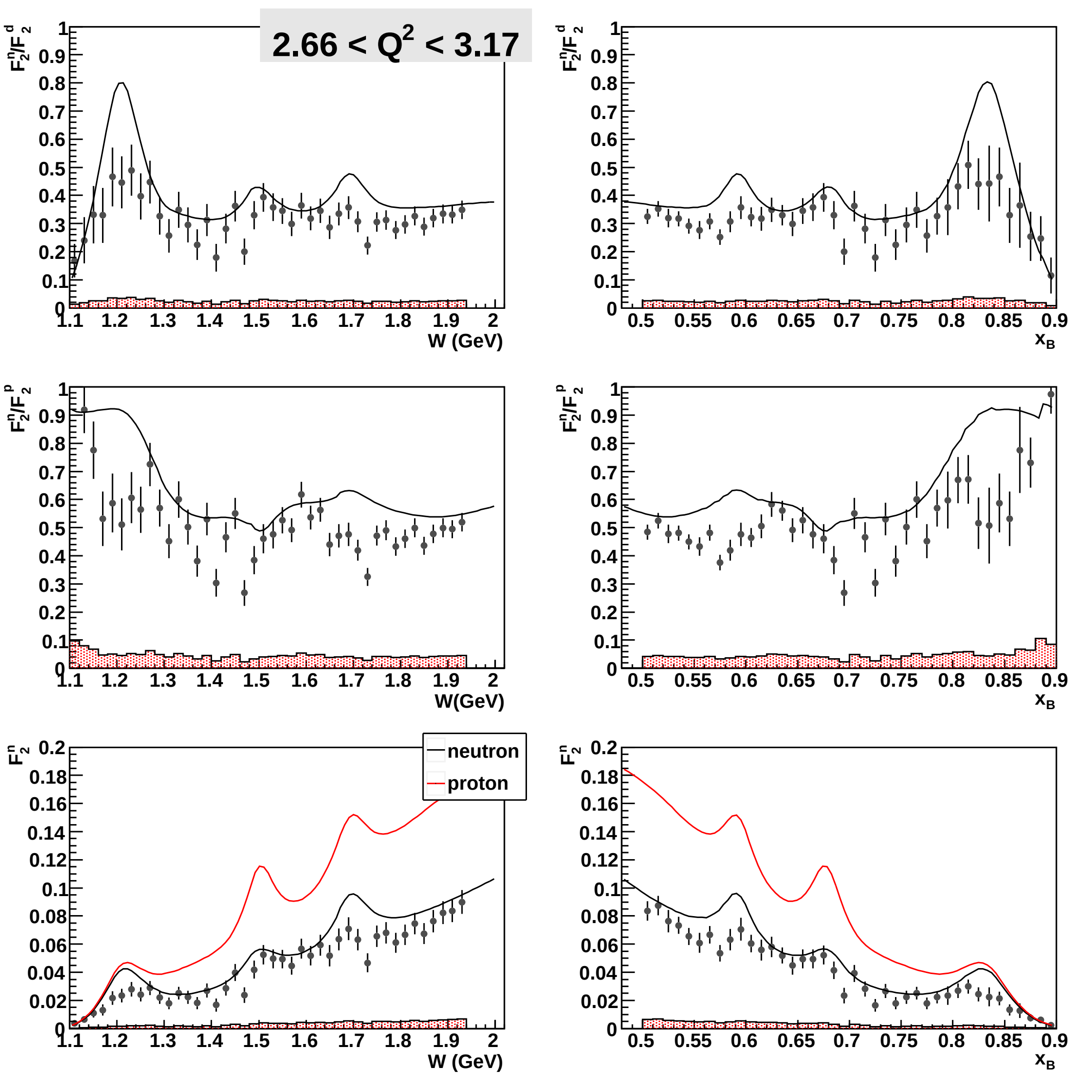

Figure 1.29: Same as Fig. 1.23 but at $2.66 < Q^2 < 3.17$ GeV^2.

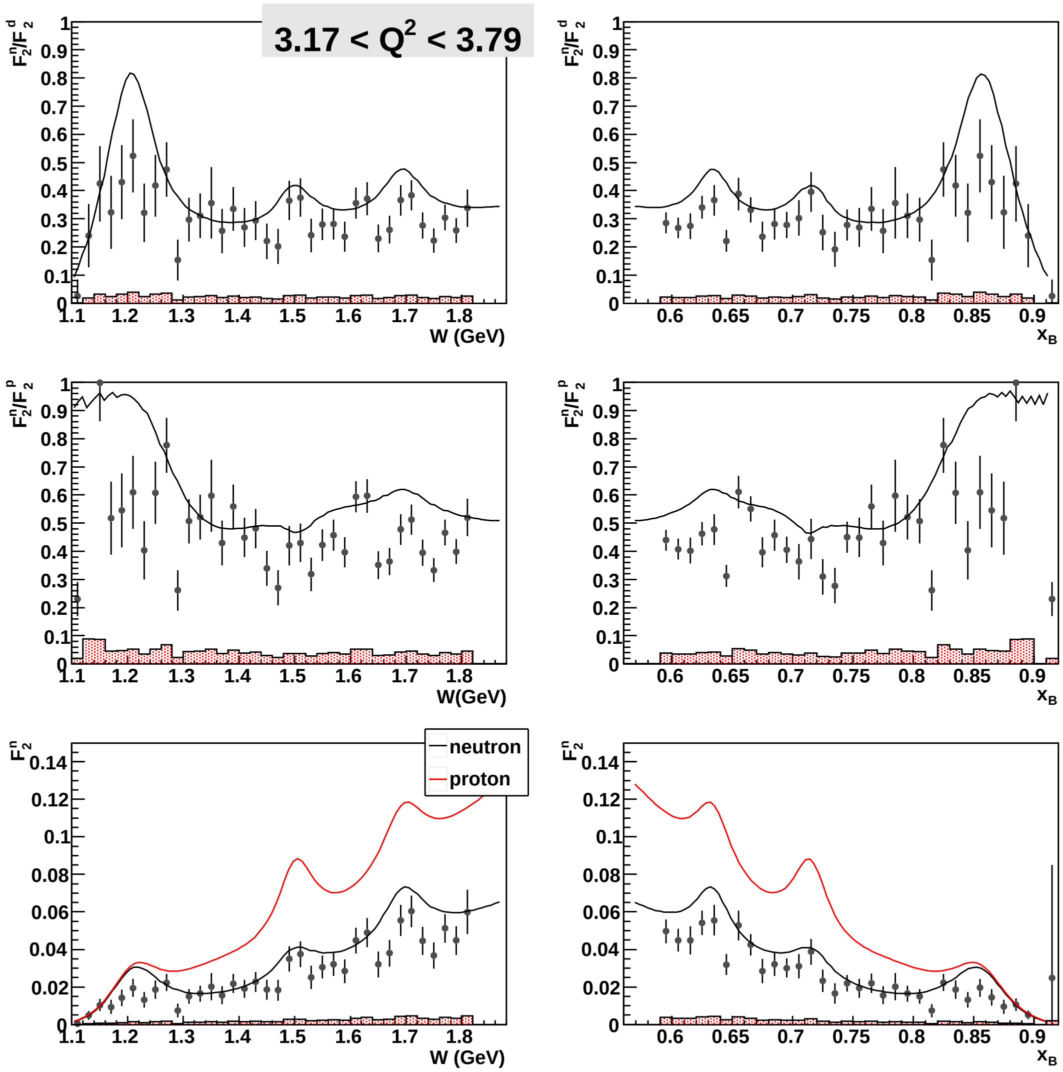

Figure 1.30: Same as Fig. 1.23 but at $3.17 < Q^2 < 3.79$ GeV^2.

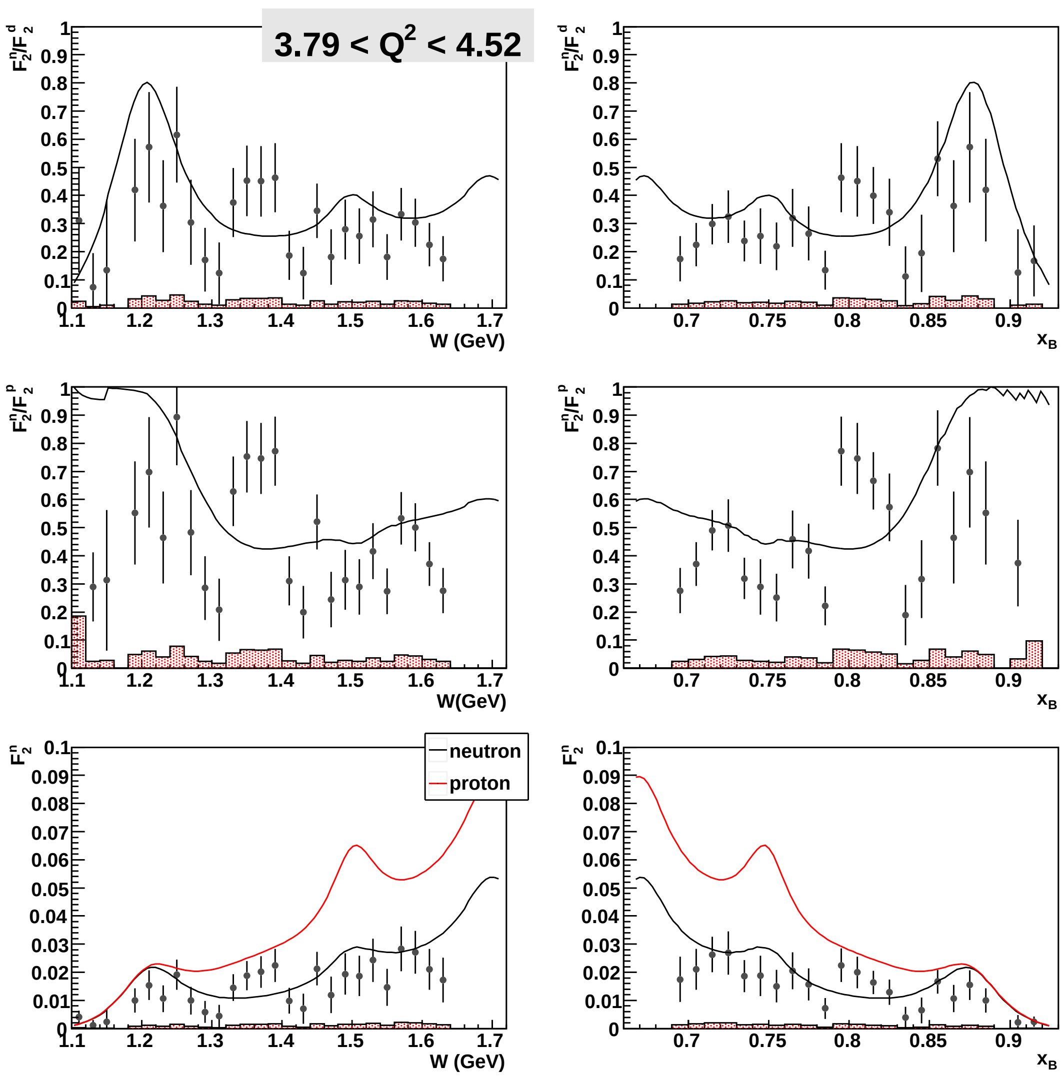

Figure 1.31: Same as Fig. 1.23 but at $3.79 < Q^2 < 4.52$ GeV^2.

1.3 The MC Method

In order to understand better the off-shell and final-state-interaction corrections to the tagged data and to check systematic errors, we have performed a second analysis of the BoNuS data set using the tagged events compared to a plane-wave impulse approximation (PWIA) spectator model. Deviations of the data from the model indicate the magnitude and kinematic dependence of off-shell corrections to the structure function F_{2n}^{eff} and the importance of rescattering in the final state as well as target fragmentation.

1.3.1 Generating events

Simulated events used in this analysis were generated using a Plain Wave Impulse Approximation (PWIA) generator for inclusive electron scattering on moving nucleons inside deuterium. This generator was developed and used for the first spectator tagging experiment with CLAS, e6 [1]. The generator is based on the RCSLACPOL code developed at SLAC [2]. It uses up-to-date nucleon form factors [3] and structure functions [4, 5] as well as the Mo-Tsai [6] prescription to calculate both Born and radiated cross sections for inclusive electron scattering on a single nucleon. These cross sections are then transformed (obeying proper relativistic kinematics) from the nucleon rest system into the lab, using the Paris wave function [7] to describe the momentum distribution of nucleons inside deuterium. This generator works in the "extreme spectator approximation" and does not assume any interaction of the final state debris of the struck nucleon with the spectator, which escapes with its initial momentum, nor any off-shell or EMC-type effects on the nucleon structure functions.

The three purposes for which we needed simulated events in the MC analysis are: subtracting the radiative elastic tail from the inelastic event distribution, accounting for detector acceptance and resolution, and comparing the *inclusive* experimental data with the MC prediction to derive an "empirical electron efficiency". To satisfy these needs, three kinds of events were generated:

1. simulation of quasi-elastic scattering of electrons off the neutron inside deuterium in the

plane wave spectator approximation including electromagnetic radiative effects,

2. simulation of inelastic scattering off the neutron in the same framework (with radiative effects),

3. Fully inclusive scattering $d(e,e')X$ off the deuteron (with radiative effects).

Events with quasi-elastic scattering of the electron off a moving neutron in the spectator picture are produced as follows. Initially, the electron is assigned random kinematics within the boundaries (Q^2 and ν) defined in the configuration file. In the spectator picture, the energy and momentum of the off-shell bound nucleon (E_N and $\vec{p}_N$) are related to the spectator nucleon momentum $\vec{p}_s$ as

$$E_N = M_D - \sqrt{M_p^2 + p_s^2} \tag{1.15a}$$

$$\vec{p}_N = -\vec{p}_s, \tag{1.15b}$$

and the target nucleon (off-shell) mass is

$$M^* = \sqrt{(M_D - \sqrt{M_p^2 + p_s^2})^2 - p_s^2}. \tag{1.16}$$

The initial momentum of the struck nucleon is distributed according to

$$P(\vec{p}_N) = |\psi(\vec{p}_N)|^2, \tag{1.17}$$

where $\psi(\vec{p}_N)$ is the Paris deuteron wave function [8, 7] rescaled using light-cone formalism [9]. The events were then generated according to the elastic cross-section given by the usual Rosenbluth formula in the rest frame of the target nucleon, with the “cross section type” form factors from Arrington et al. [3]. The elastic radiative tail is calculated using the full prescription of Mo and Tsai [6]. The reduction of the quasi-elastic peak itself due to the internal radiation is given by

$$\left(\frac{d\sigma}{d\Omega}\right)_{rad} = e^{\delta}\left(\frac{d\sigma}{d\Omega}\right)_{Born}, \tag{1.18}$$

where the expression for the parameter δ is given in [6]. The event generator also simulated external radiative energy loss *before* scattering due to material in the beam.

The inelastic data were generated similarly to the quasi-elastic data. The cross-section was evaluated using

$$\frac{d\sigma}{dE'\,d\Omega} = \left(\frac{d\sigma}{d\Omega}\right)_{Mott} \frac{2MxF_2(x,Q^2)}{\epsilon Q^2} \frac{1+\epsilon R(x,Q^2)}{1+R(x,Q^2)}, \tag{1.19}$$

where $R = \sigma_L/\sigma_T$, σ_L and σ_T being the longitudinal and transverse cross-sections. The polarization of the virtual photon, ϵ, is given by

$$\frac{1}{\epsilon} = 1 + 2\left(1 + \frac{Q^2}{4M^2x^2}\right)\tan^2\frac{\theta}{2}. \tag{1.20}$$

The proton and neutron structure functions F_2 and R were taken from fits by Bosted *et al.* [4, 5] to world proton and deuteron data, including data from Jefferson Lab's Hall B and C. The fit is constrained to merge with the New Muon Collaboration (NMC) fit to SLAC, BSDMS and NMC data on the proton and deuteron structure functions [10] at large W. Radiative effects were simulated using the output of the SLACPOLRAD program [2]. SLACPOLRAD calculates the ratio of radiated to Born (unradiated) cross-section for DIS without the elastic tail. These ratios were applied to scale the generated unradiated cross-section.

The fully inclusive events were generated by adding quasi-elastic and inelastic events from both the neutron and the proton (integrated over all spectator momenta), plus the radiative elastic tail from $D(e,e')D$. A small empirical correction was applied to bring the simulated cross section for $D(e,e')$ into better agreement with the most recent data from Hall C (not published yet - M.E. Christy, private communication).

1.3.2 Detector simulation

The generated events were run through a full simulation of the experimental setup, including external radiation losses. The target and RTPC part of the setup were simulated in full detail using a GEANT4-based [11] simulation package written for our experiment (the same simulation that was used for the RTPC momentum corrections, see section **??**). The standard CLAS part of the setup was simulated using GSIM. First, particle paths through the RTPC were simulated. The output information (position and momentum vectors of all particles at the boundary) was written to files which served as input for the GSIM package. To simulate inefficiencies of the CLAS detector, the output of GSIM was fed to the GSIM Post Processing package (GPP), which accounted for such things as finite resolution of DC and SC, broken DC wires, etc.

After the generated events went through the simulated detectors, we obtained files with simulated detector responses for the generated events. Finally, these files were processed by the usual data processing program (RECSIS), the same one that was used for processing experimental events. All the same cuts were applied as for the real data, except for the CC and EC cuts, since the CC and EC response were difficult to simulate accurately (see below). Since the simulated detector in GEANT4/GSIM is “ideal”, many of the empirical corrections we had to apply to our data where not needed and therefore left out for the simulated data analysis. In particular, only the first of the RTPC momentum corrections was used (see **??**); no radius of curvature rescaling was applied. Similarly, the full CLAS momentum correction was not used; only the energy loss correction was applied. No accidental background subtraction was applied to the simulated data since they did not contain any background.

The outputs of RECSIS for experimental and simulated events were directly compared and used in the analysis. Figures 1.32 and 1.33 show plots of the W and W^* distributions for quasi-elastic 4 and 5 GeV beam energy simulations, respectively, as examples of simulation results. The same distributions for *in*elastic simulations can be found in Figs. 1.34 and 1.35.

All simulated events that passed the experimental cuts were filled into an array of structures identical to those for the experimental data (see below) for further processing.

1.3.3 Empirical Efficiency Correction

As stated above, the simulated data analysis did not use the standard CC and EC cuts since the acceptance/calibration of these detectors was not fully understood. In particular, the hardware

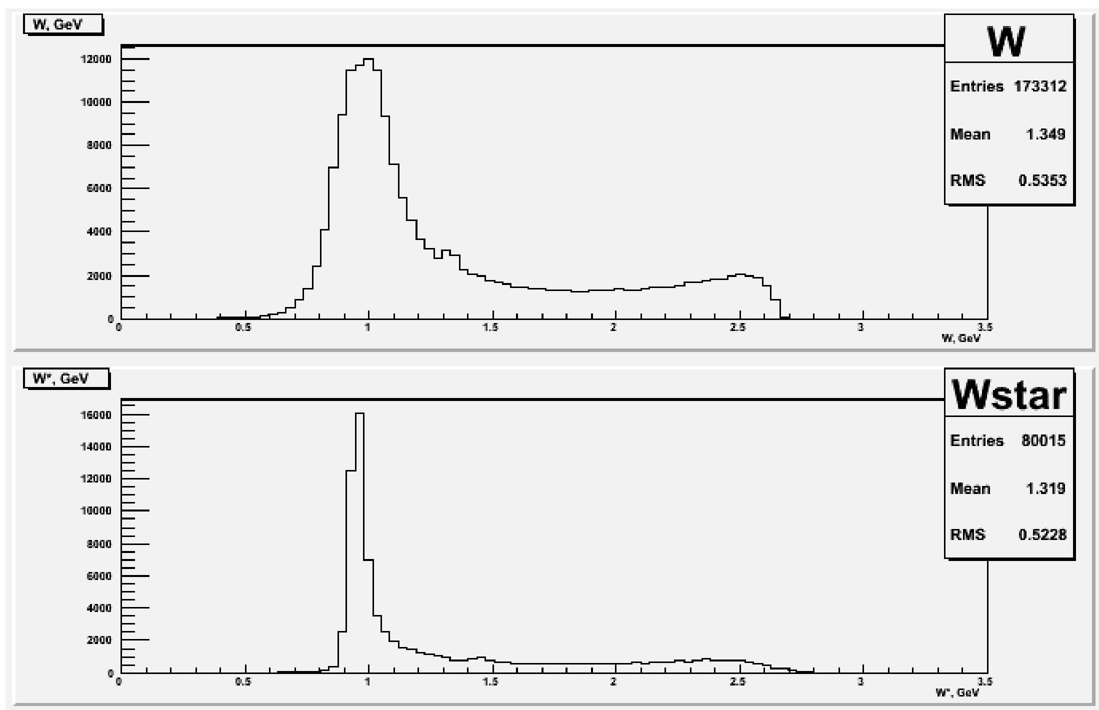

Figure 1.32: The W and W^* distributions of the quasi-elastic simulation for the 4 GeV data.

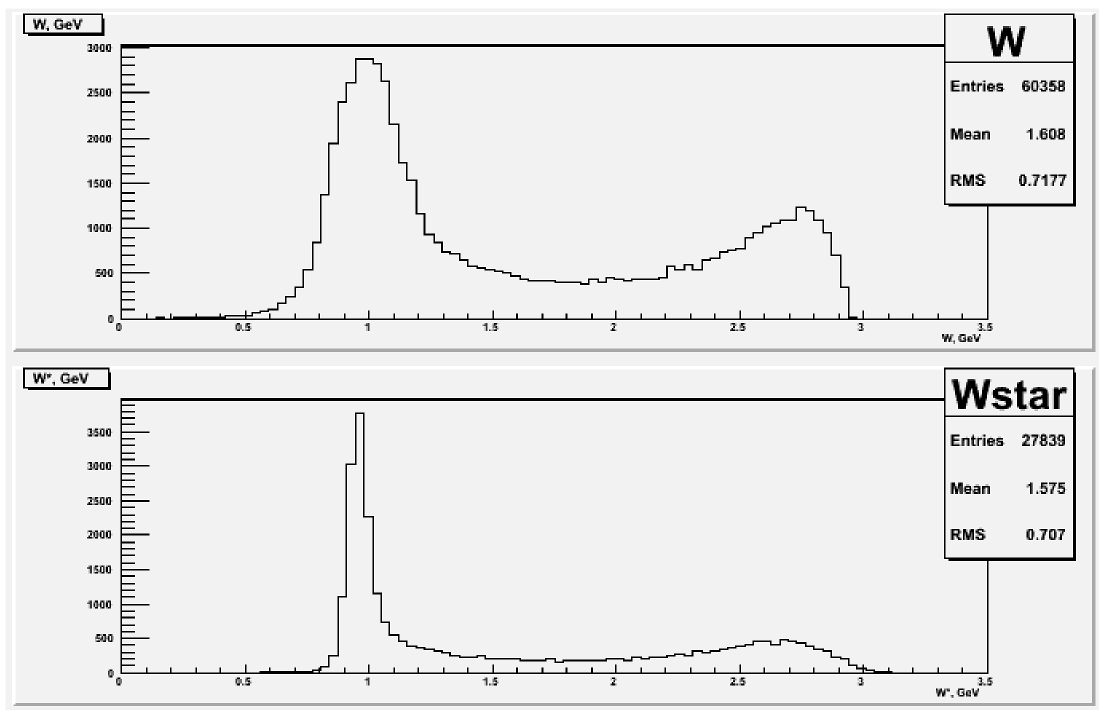

Figure 1.33: The W and W^*distributions of the quasi-elastic simulation for 5 GeV beam energy.

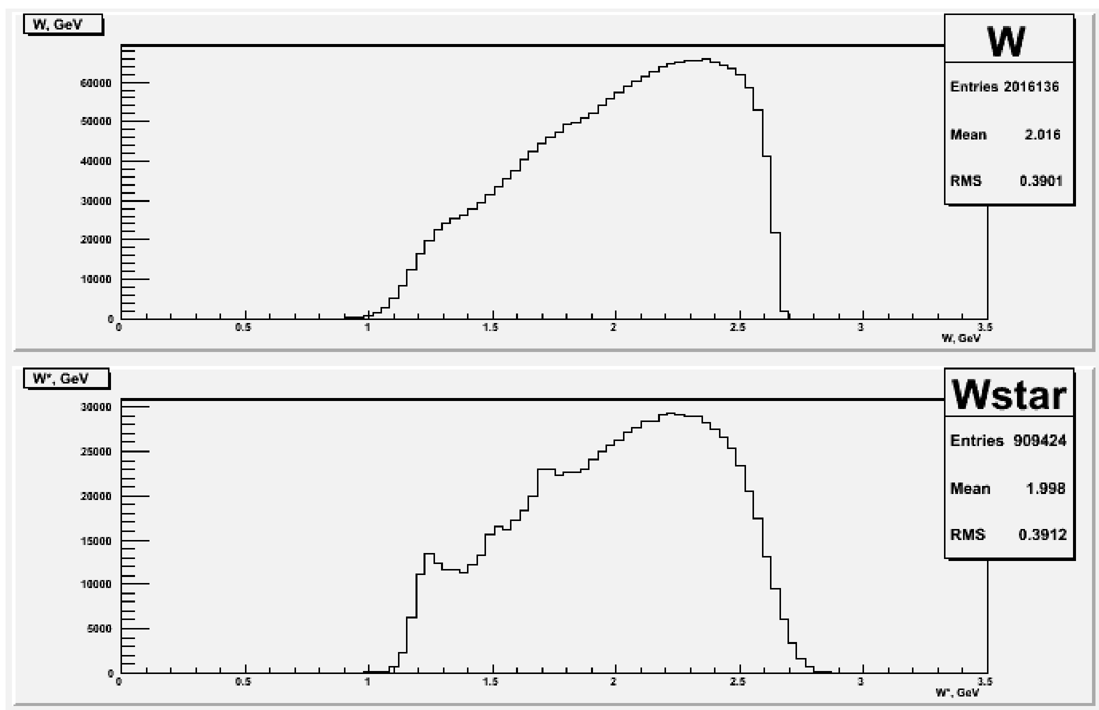

Figure 1.34: The W and W^* distributions of the inelastic simulation for the 4 GeV data.

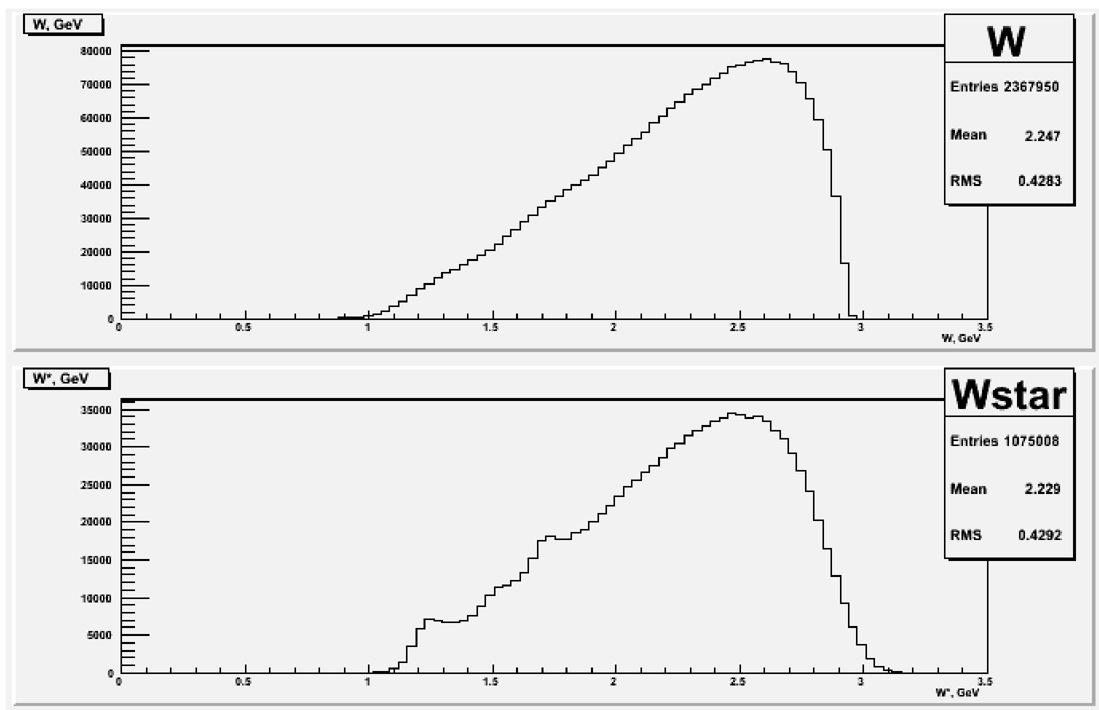

Figure 1.35: The W and W^*distributions of the inelastic simulation for 5 GeV beam energy.

threshold for the EC trigger input was set rather high and varied throughout the experiment. The CC was never properly calibrated and also had a rather high threshold. Instead of trying to simulate the efficiency of these detectors and deduce the corresponding electron ID cuts (as well as the trigger and overall tracking efficiency), we used our simulation of fully inclusive D(e, e') data in comparison with the same kind of data from the experiment to derive an "empirical efficiency correction". The fully inclusive events (both data and simulation) were binned in trigger electron energy and polar scattering angle, E' and θ, (ignoring any spectator tracks in the RTPC). The inclusive simulation did not have any CC and EC cuts, either, while all the usual electron cuts from the tagged analysis were applied to the inclusive experimental data. Corrections for contamination of the experimental data by pair-symmetric ("e^+/e^-") and mis-identified pion background were applied as described in Section 1.2.3. The ratio of the distribution of scattering angles and energies of the inclusive experimental data over that of the simulated electrons yields the "empirical electron efficiency" as a function of scattering angle and energy. This efficiency was used in the main analysis by weighing simulated counts and thus compensating our lack of understanding of the detector efficiency. Because the simulation of fully inclusive electrons is based on the same generator, cross section equations and detector simulation as the tagged data, common factors relating input structure functions and measured electron distributions cancel out in this procedure, much reducing systematic uncertainties on the simulation.

Figure 1.36 shows the results of this procedure in a one-dimensional projection. The top panel shows the experimental data binned *vs.* W, while the second panel shows the simulated inclusive data, and the third panel shows both curves overlaid after proper normalization. This is our worst case, since the 2 GeV data were taken during a time of the run when we were still changing EC and CC thresholds. Since no cuts on EC or CC are contained in the simulation, it does not fall off as quickly at high W (low E') as the data. The ratio of the red over the blue curve would then correspond to our "empirical efficiency" which can correct the tagged data for this discrepancy. Figures 1.37,1.38 repeat the lower panel of Fig. 1.36 for the other two beam energies.

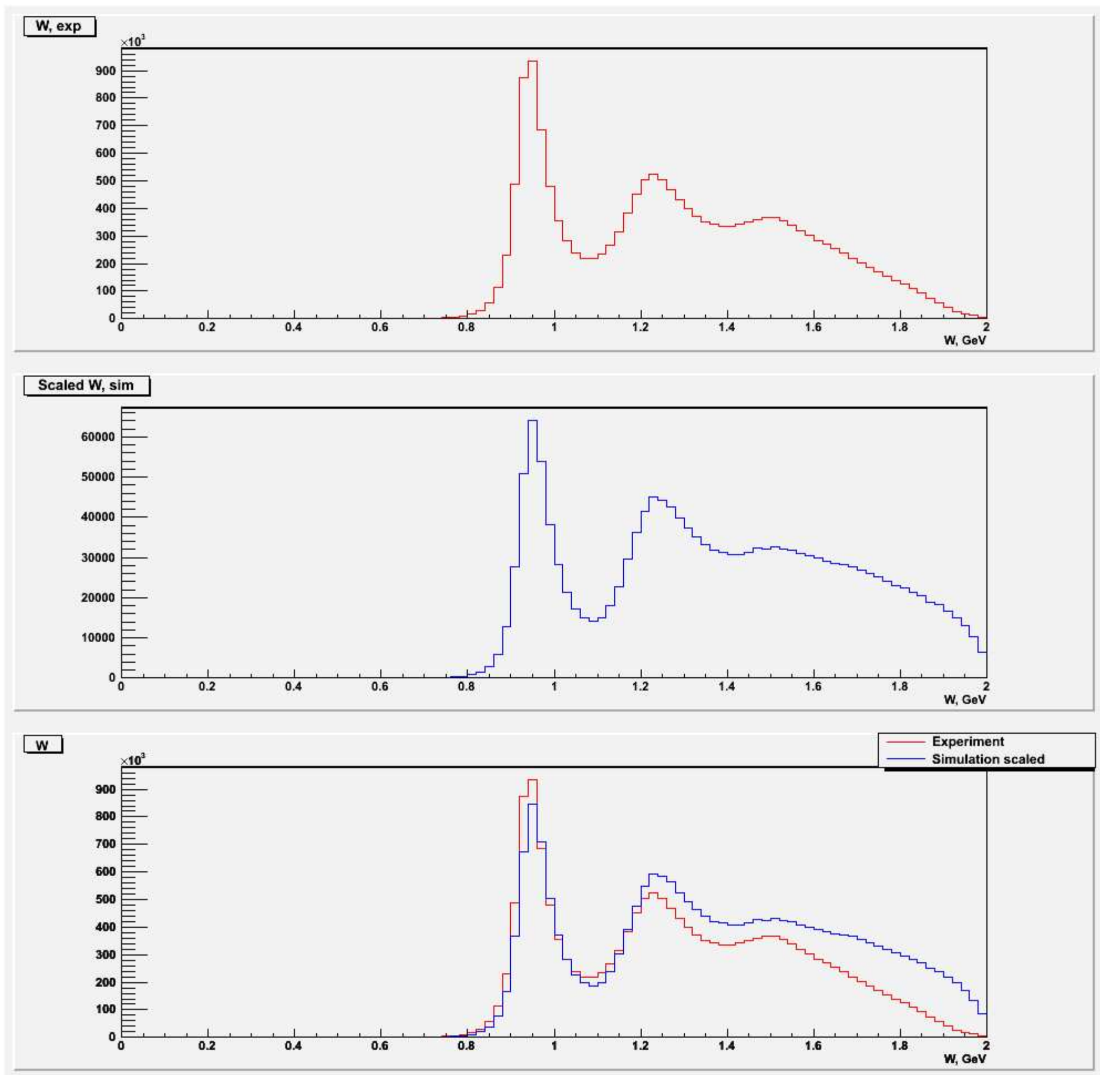

Figure 1.36: Inclusive W distributions for experimental (red) and simulated (blue) data. Simulated data were scaled by a factor of 13.2 to account for the difference between experimental and simulated luminosity. The beam energy is 2.140 GeV.

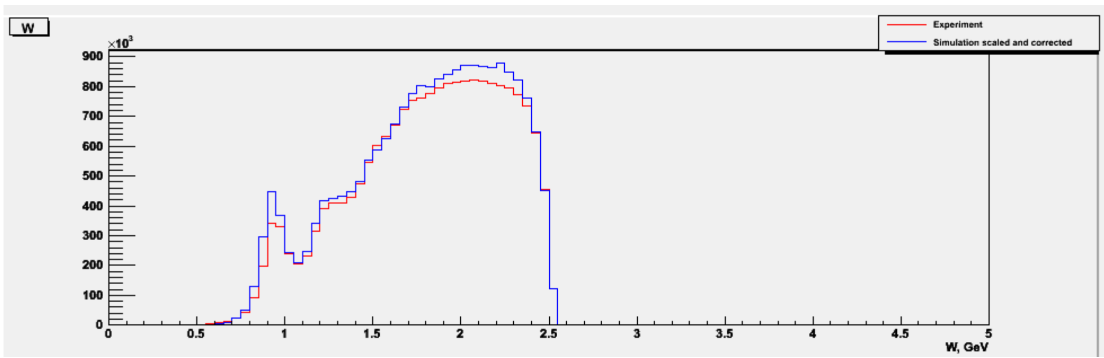

Figure 1.37: Same as Fig. 1.36 for a beam energy of 4.2 GeV.

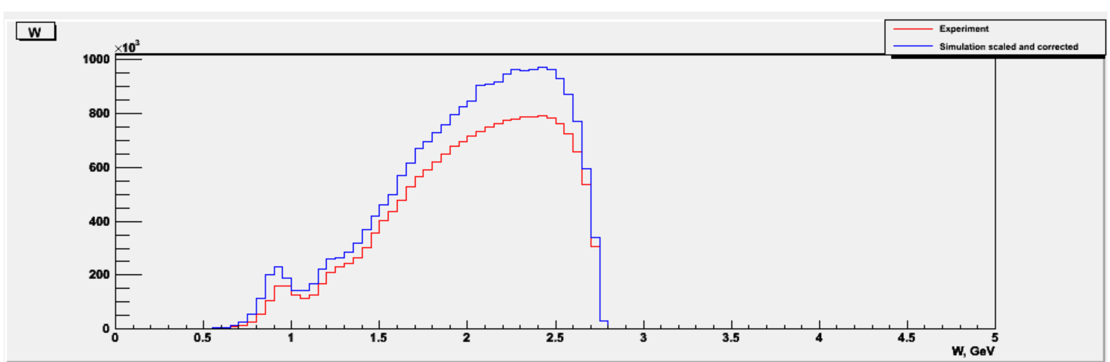

Figure 1.38: Same as Fig. 1.36 for a beam energy of 5.3 GeV.

1.3.4 Background Subtraction

Events were considered to be good electron - RTPC proton coincidences if the z-distance between the reconstructed vertices of those two particles, $\Delta z = z_{el} - z_{pr}$ was less than 15 mm. Unfortunately, there were events with random coincidences, in which the trigger electron and an unrelated RTPC proton were within the aforementioned 15 mm. This accidental background needed to be estimated.

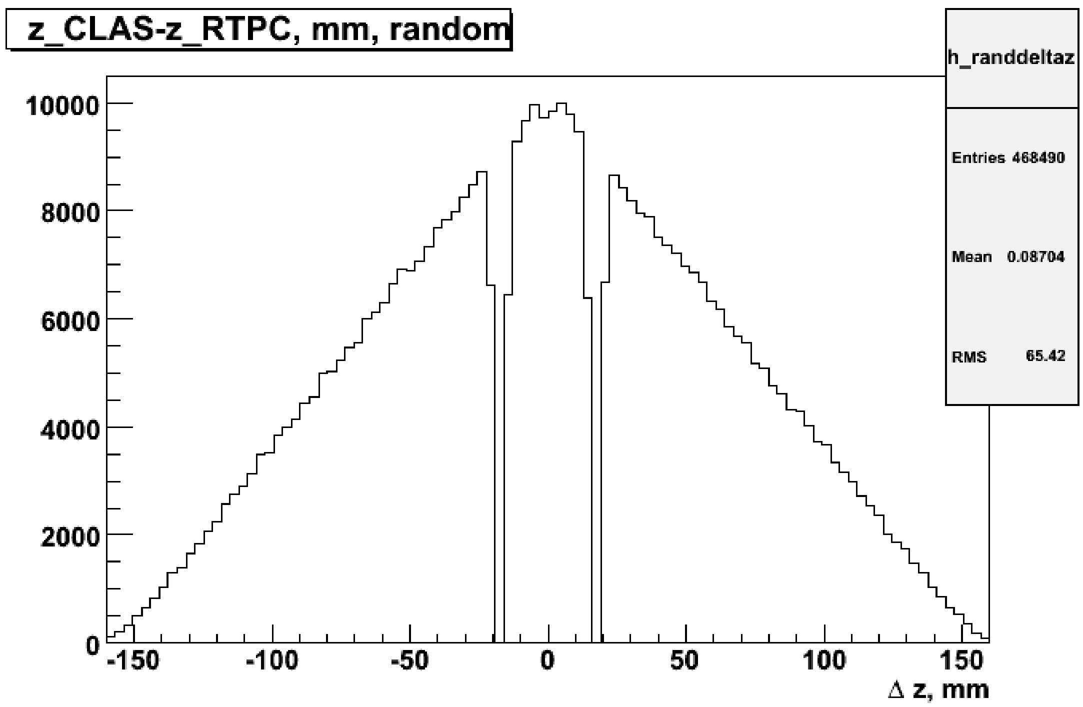

Figure 1.39: A representative plot of random coincidences Δz distribution for 5 GeV data. The shown plot is for Q^2 between 1.10 and 2.23 $(GeV/c)^2$, W^* between 1.35 and 1.60 GeV, and p_s between 70 and 85 MeV/c. Gaps between 15 and 20 mm are present, since events in which Δz was in that range belonged neither to the area under the peak nor to "wings" (see text for the explanation), and thus were ignored.

Random coincidences were emulated by taking the trigger electron from one event and the RTPC proton from another. Thus, they were guaranteed not to come from a real physics event. Using information from the chosen electron-proton random pair, all quantities in which real data were binned, Q^2, W^*, x^*, and $\cos(\theta_{pq})$, were calculated, and the coincidence was assigned to the corresponding bin. If the distance between the vertices of the electron and the proton, Δz, was less than 15 mm, the event would emulate a random coincidence under the signal. If Δz was larger than 20 mm, this was considered a "wing" event, that could not be confused with the signal. Then, after going over all the events, we could form a ratio of the number of coincidences under the signal and the number of "wing" events for each of our bins. A sample of the distribution of random coincidences is shown in Fig. 1.39; one can clearly see the expected triangular shape (see Section 1.2.1).

The following Figs. 1.40,1.41 show the (slight) variation of these distributions with selected kinematic variables, $\cos(\theta_{pq})$ and W. Using both wings averaged out any small distortions in the triangular shape, leading to a ratio for the area under the peak to the integrated wings, R_{bg}, which did not vary significantly with any kinematic variable and fluctuated (statistically) between 0.23 and 0.25

All experimental coincidences between electrons and RTPC protons were separated into the same categories, "wing" events (those with $|\Delta z| > 20$ mm) and "signal" (peak) events (those with $|\Delta z| < 15$ mm). Then, the number of "wing" events was converted to the number of random coincidences under the peak by multiplying it by the aforementioned ratio R_{bg} of random under-the-peak to random "wing" events. The resulting accidental background events were subtracted from the events within the peak for each kinematic bin.

The resulting fraction of background events ranged from somewhat below 10% to over 20%, depending on the kinematic bin. Figure 1.42 shows, for example, the dependence of the background fraction on the invariant mass W^* of the final state. The background is mostly flat around 17%, but decreases in the region of narrow peaks (most prominently in the region of the Delta, $W = 1.23$ GeV) where the signal is larger, and increases at the edges of the kinematic acceptance, where "real" coincidences are rarer.

In addition, backgrounds due to pions misidentified as electrons (passing all cuts) as well as pair-symmetric contamination of the electron sample were also corrected for in similar fashion as discussed for the ratio method. (Section 1.2).

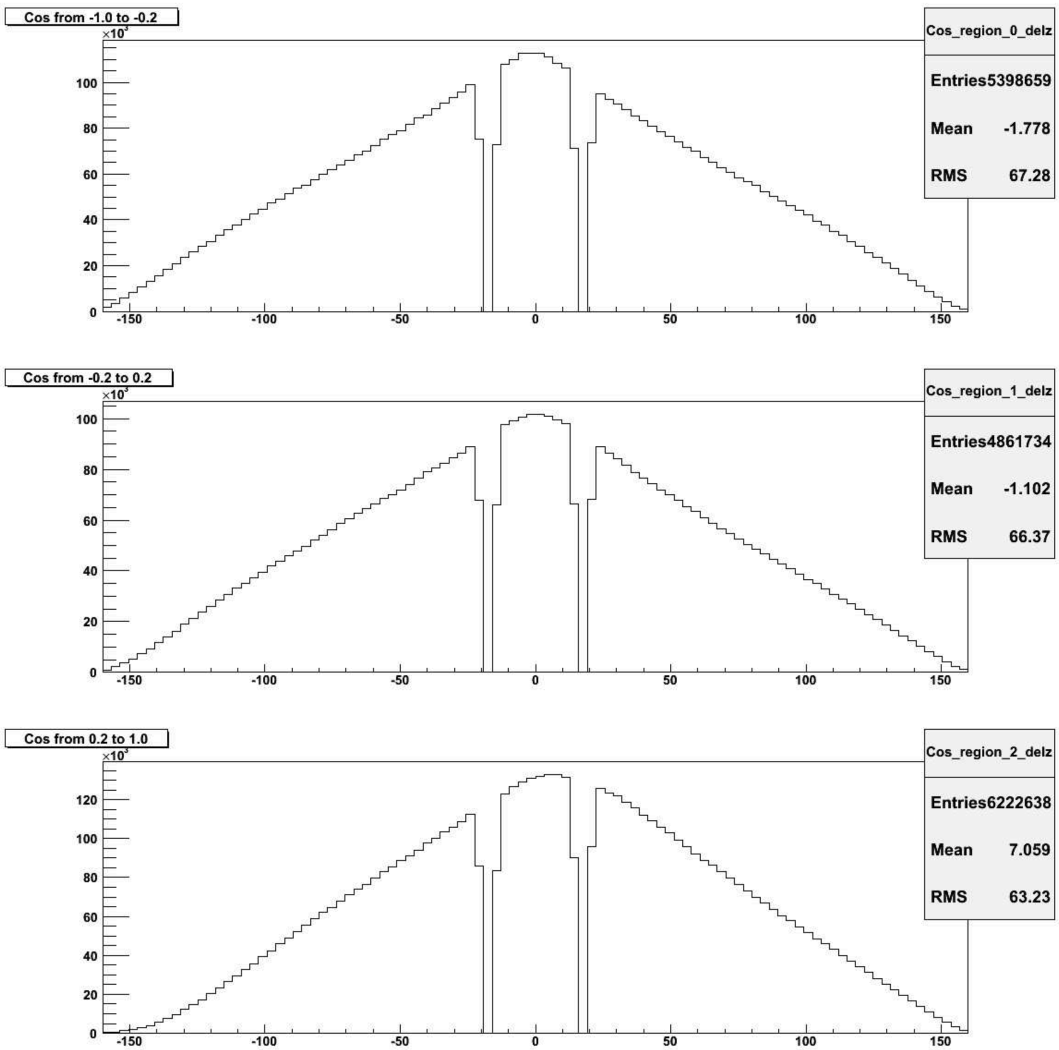

Figure 1.40: Similar to Fig. 1.39. The Δz distributions are shown for three different bins in the angle $\cos\theta_{pq}$. Careful inspection shows that for backward angles (top panel) more random protons are at larger z than the electron vertex (left "wing") since the "backward" acceptance of the RTPC is of course larger for protons coming from more downstream parts of the target. The situation is reversed for forward angles (bottom panel). However, averaging over both wings gives very nearly the same ratio to the central peak, leaving R_{bg} unchanged.

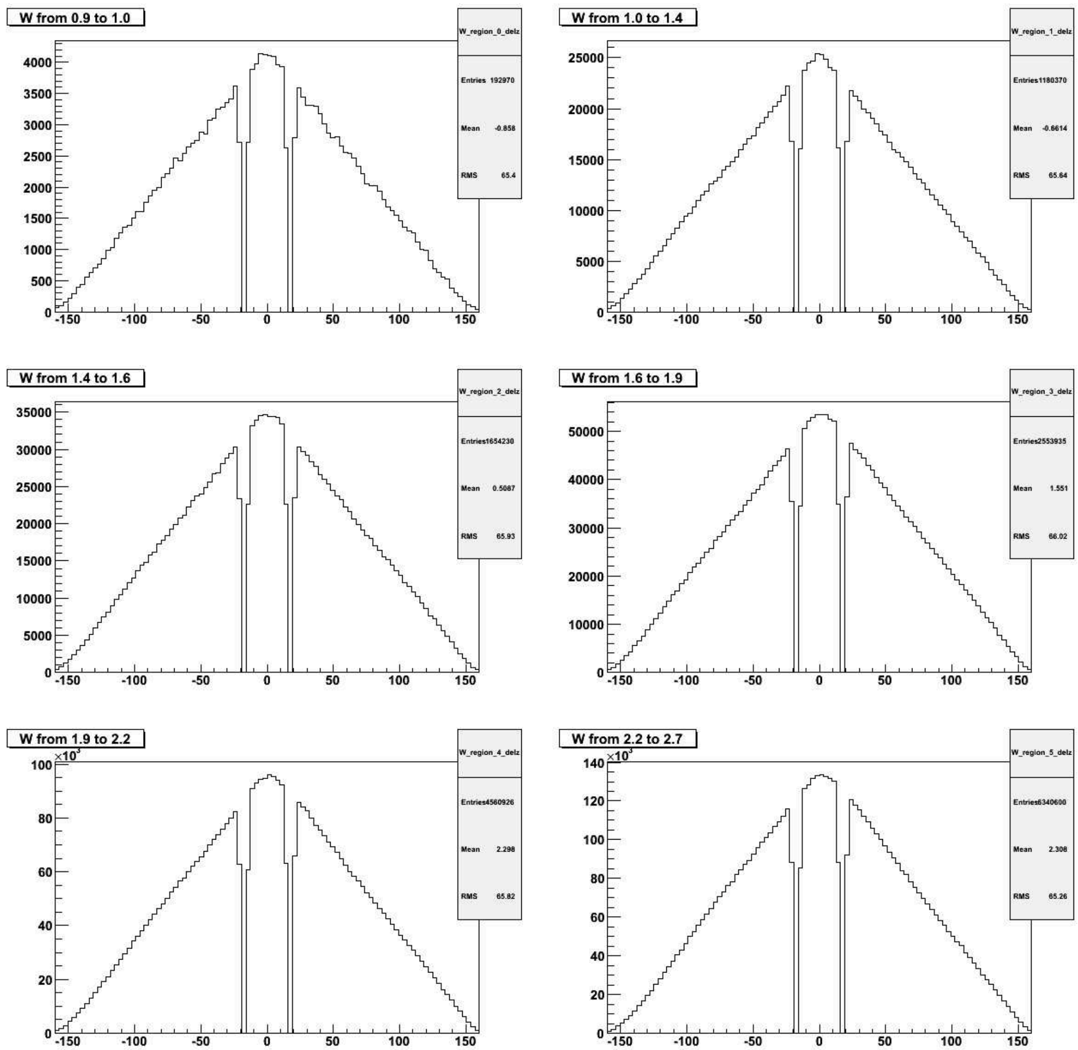

Figure 1.41: Similar to Figs. 1.39,1.40. The Δz distributions are shown for six different bins in the invariant final state mass W^*. Practically no systematic differences are visible.

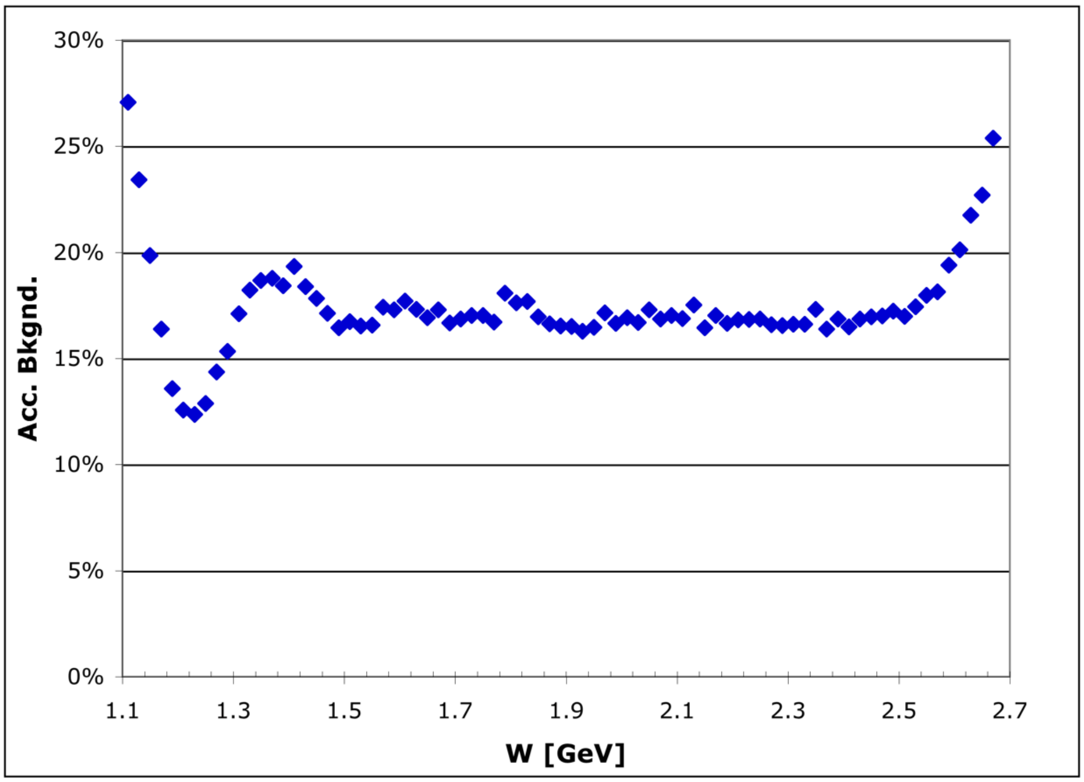

Figure 1.42: Fraction of accidental coincidence background inside the cut $|\Delta z < 15 \text{ mm}|$ as a function of the invariant final state mass W^*. See text for explanation.

1.3.5 Binning

A loop over all experimental events that passed the cuts (see section **??**) was performed. If an event was tagged, the W^*, Q^2, $\cos(\theta_{pq})$, and spectator momentum bins corresponding to the values recorded in the structure were found. Binning in W^* is performed twice: once with 6 bins for studying the dependence of our results on other variables for events belonging to each of these 6 bins, and once with 90 bins, for plotting structure functions *vs* W^*. In the same fashion 2 possible sets of $\cos(\theta_{pq})$ bins were made: 3 bins for making plots *vs.* other variables, and 10 bins for making plots with $\cos\theta_{pq}$ plotted on the horizontal axis. In detail, we use the following bins:

- $\cos(\theta_{pq})$ bins:
  - "Small" bins: 10 equal bins between -1 and 1.
  - "Big" bins: 3 bins, lower bounds being: -1.0, -0.2, 0.2, upper bounds being -0.2, 0.2, 1.0.
- Spectator momentum bins - 4 bins, lower bounds: 0.07, 0.085, 0.1, 0.12 GeV; upper bounds: 0.085, 0.1, 0.12, 0.15 GeV.
- Q^2 bins:
  - For 2 GeV beam energy: 3 bins, lower bounds: 0.2227, 0.4524, 0.7697 GeV/c; upper bounds: 0.4524, 0.7697, 1.0969 GeV/c.
  - For 4 GeV beam energy: 3 bins, lower bounds: 0.7697, 1.0969, 2.2277 GeV/c; upper bounds: 1.0969, 2.2277, 4.5243 GeV/c.
  - For 5 GeV beam energy: 2 bins, lower bounds: 1.0969, 2.2277 GeV/c; upper bounds: 2.2277, 4.5243 GeV/c.
- W^* bins:
  - "Big" bins, for plotting other variables - 6 bins, lower bounds: 0.88, 1.00, 1.35, 1.60, 1.85, 2.20 GeV; upper bounds: 1.00, 1.35, 1.60, 1.85, 2.20, 2.68 GeV.

– "Small" bins, for horizontal axis - 90 bins of width 20 MeV equally spaced between 0.88 and 2.68 GeV.

Alternatively to binning in small bins of W^*, we also binned all data in bins of

$$x^* = \frac{Q^2}{2E_N \cdot \nu + 2\vec{q} \cdot \vec{p_s}} \tag{1.21}$$

to extract the functional dependence of F_{2n} on x^*. 40 equidistant bins between 0 and 1 were used.

As a result of the binning procedure four arrays are filled: tag_counts_exp - "small" bins in $\cos(\theta_{pq})$, "big" bins in W^*; tag_byreg_exp - "big" W^* bin, "big" $\cos(\theta_{pq})$ bin, tag_wplots_exp - "small" W^* bins, "big" $\cos(\theta_{pq})$ bins, and tag_xplots_exp - small x^* bins, "big" $\cos(\theta_{pq})$ bins.

All backgrounds are evaluated bin by bin and subtracted from the counts in all of them. The same arrays were replicated once for the simulated inelastic data and once again for the simulated quasi-elastic data (with radiative tail) and filled accordingly. All simulated counts were multiplied with the trigger efficiency (that also incorporated the pion and charge symmetric contamination correction) and the empirical RTPC efficiency.

1.3.6 Extraction of F_{2n}

As a first step, the quasi-elastic radiative tail was subtracted from the experimental data as follows: The quasi-elastic simulation was cross-normalized to the data in the vicinity of the quasi-elastic peak, $0.88 < W^* < 1.00$ GeV, for each bin in Q^2, p_s and $\cos(\theta_{pq})$ and then subtracted bin-by-bin from the data at higher W^*. The cross-normalization factors are denoted as $ratio$ below. Fig. 1.43 shows the 5.3 GeV W^* spectrum for four bins in p_s at backward angles and $Q^2 = 1.66$ GeV^2. The red curves are the simulated tagged quasi-elastic events, normalized to the measured tagged events at the elastic peak.

The simulated inelastic tagged scattering events were then cross-normalized with the (background- and radiative tail-corrected) experimental data. The cross-normalization factors were found by summing experimental and simulated counts over a specific region in W^*, Q^2 and $\cos\theta_{pq}$, where according to the theoretical expectations the spectator picture should hold and nuclear uncertainties in the fits for F_{2n} used by the generator are expected to be small. These regions were selected as follows:

- For 2.1 GeV beam energy: $1.2 < W^* < 1.34$ GeV, $0.7697 < Q^2 < 1.0969$ GeV^2 and $-1.0 < \cos(\theta_{pq}) < -0.2$.
- For 4.2 GeV beam energy: $2.0 < W^* < 2.2$ GeV, $0.7697 < Q^2 < 1.0969$ GeV^2, and $-1.0 < \cos(\theta_{pq}) < -0.2$.
- For 5 GeV beam energy: $2.0 < W^* < 2.2$ GeV, $1.0969 < Q^<2.2277$ GeV^2, and $-1.0 < \cos(\theta_{pq}) < -0.2$.

These factors were found and applied separately for each spectator momentum bin, because the RTPC efficiency as a function of momentum is not completely understood. Therefore, they contain an empirical correction for the (p_s–dependent) inefficiency of the RTPC.

In the final step, the ratio of the experimental number of (background-corrected) counts to the normalized, simulated inelastic counts is formed in each bin of interest. If the cross section model used in the generator were a perfect description of the underlying physics, this ratio would be unity (within statistical and systematic uncertainties) in every bin, since we simulated all steps from (Born) cross section to (radiated) count rates and accounted for any remaining detection inefficiency by using both the empirical electron efficiency and (p_s–dependent) RTPC efficiency corrections. Any significant deviation from unity would indicate that some ingredient in the cross section formula, Eq. 1.19, differs from the ideal spectator model in the bin in question. Therefore, the ratio $R(data/MC)$ can be interpreted as

$$R(data/MC) = \frac{F_{2n}^{eff}(W^*, Q^2, \vec{p_s})}{F_{2n}^{model}(W, Q^2)}, \tag{1.22}$$

where the "effective structure function" $F_{2n}^{eff}(W^*, Q^2, \vec{p_s})$ also accounts for corrections to the PWIA spectator picture from FSI and target fragmentation. By multiplying the ratio with the value F_{2n}^{model} evaluated at the bin center, we can get the (bin-centered) value for the effective

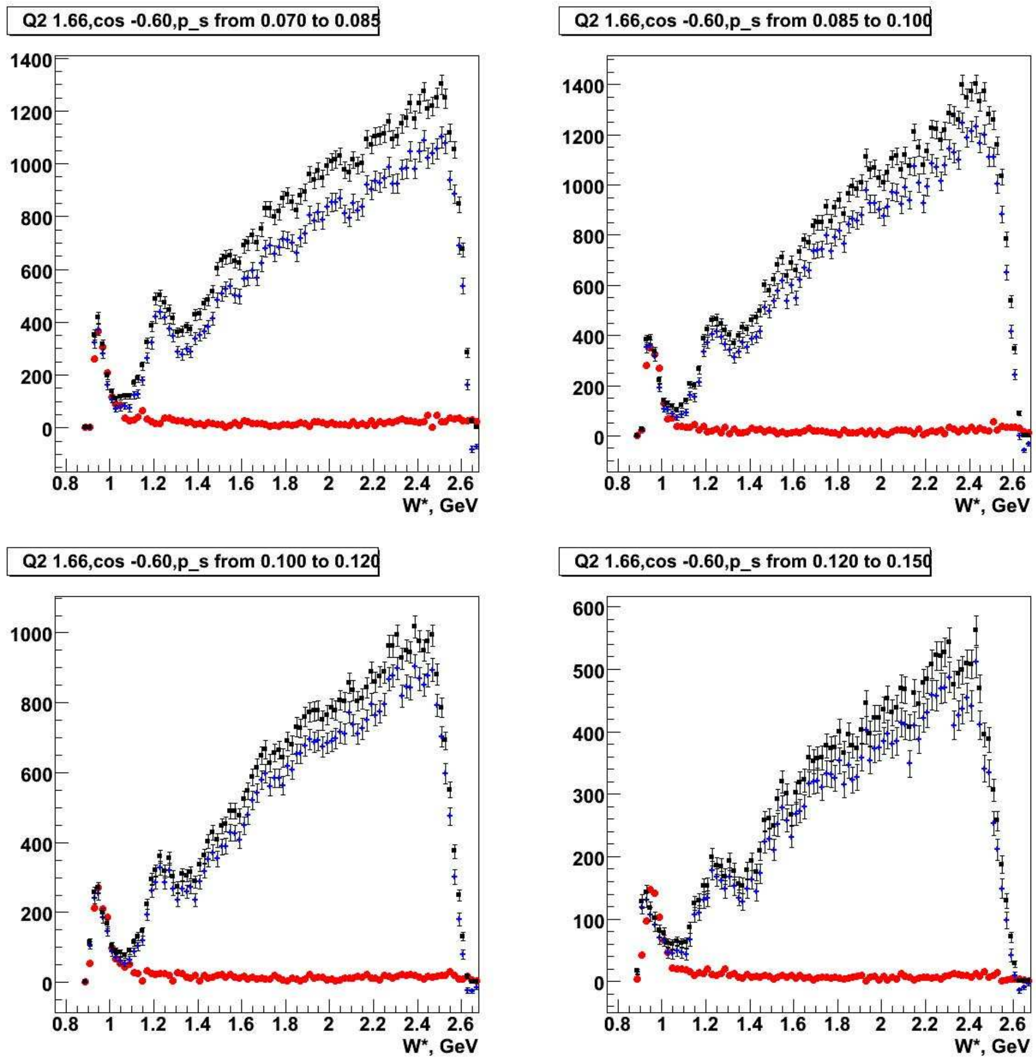

Figure 1.43: Raw tagged data (black squares), tagged data with subtracted accidental background (blue crosses), and simulated, cross-normalized elastic events (red circles). Four typical p_s bins are shown for $\langle Q^2 \rangle = 1.66$ GeV^2 and $\langle \cos\theta_{pq} \rangle = -0.60$. The beam energy is 5.262 GeV.

structure function $F_{2n}^{eff}(W^*, Q^2, \vec{p_s})$. This quantity is what we are ultimately interested in—it contains both the deviations from the spectator picture (through the dependence of F_{2n}^{eff} on $\vec{p_s}$ and θ_{pq}) and the "true" neutron structure function, where the spectator picture is accurate.

1.3.7 Systematic errors

The systematic errors for the MC Method are discussed below.

- $\boldsymbol{E' - \theta}$ **dependent acceptance and efficiency error.** This is the uncertainty on the estimate of the detection efficiency of the CLAS trigger electrons (see above). The efficiency of the detection was found as a function of E', the energy of the scattered electron, and θ, the electron scattering angle. By performing a two-dimensional bi-linear fit of the efficiency as a function of these two variables, and estimating point-to-point fluctuations in the efficiency, the $E' - \theta$-dependent uncertainty was found to be about 8.5$\%$. This means that the value of the experimental to simulated data ratio for a given bin is assigned an additional error equal to the value of the ratio multiplied by 0.085 due to the uncertainty in the trigger electron detection efficiency.

- F_{2n} **model dependence.** The simulations used in this research utilized an input model F_{2n}. The systematic error due to this model dependence was estimated to be 5$\%$ at the normalization point (where the spectator picture should hold and nuclear corrections are minor).

- **Monte-Carlo simulations.** The ratio of the experimental to the simulated data was found for each bin as

$$ratio = \frac{exp - bg - elas\_tail}{inelsimcount}, \tag{1.23}$$

where exp is the experimental data count for the bin, bg is the accidental background, $elas\_tail$ is the normalized elastic tail found using simulated data, $inelsimcount$ is the number of counts in this bin from the simulated data multiplied by the trigger electron detection efficiency and cross-normalized with the experimental data count. The error on this quantity due to the uncertainty in Monte-Carlo (MC) counts can be found by chain differentiation as

$$\Delta ratio_{MCcount} = \frac{\partial(ratio)}{\partial(MCcount)}\Delta MCcount, \tag{1.24}$$

where $\Delta ratio_{MCcount}$ is the uncertainty on the ratio due to the MC count uncertainty and $MCcount$ is the number of MC counts in the bin. The uncertainty found consisted of two parts:

1. **Monte-Carlo statistics.** The error due to the simulation statistics was found for each bin for the experiment to simulation ratio according to

$$error^2 = \left(\frac{elsimcount}{inelsimcount}\right)^2 /pure\_elas\_count + \frac{ratio^2}{pure\_inelas\_count}, \tag{1.25}$$

   where $elsimcount$ is the cross-normalized with experiment number of events in this bin from the elastic simulation, $inelsimcount$ is the cross-normalized with experiment number of events in this bin from the inelastic simulation, $ratio$ is the aforementioned experiment to simulation ratio for the bin, $pure\_elas\_count$ is the number of events from the elastic simulation for this bin, and $pure\_inelas\_count$ is the number of events from the inelastic simulation for this bin.

2. **Monte-Carlo systematics.** A systematic error due to the simulation was found as

$$error^2 = \left(\frac{0.1\ elsimcount}{inelsimcount}\right)^2, \tag{1.26}$$

   where $elsimcount$ is the cross-normalized with experiment number of events in this bin from the elastic simulation, $inelsimcount$ is the cross-normalized with experiment number of events in this bin from the inelastic simulation. The factor of 0.1 is the potential cross-normalization error between quasi-elastic simulation and experimental data, due to a somewhat different shape in W^* of the corresponding quasi-elastic peaks (see figure 1.43).

- **Charge-symmetric and pion contamination.** Even though careful analysis was performed to separate trigger electrons from negative pions, the latter could still be counted in as good electrons. Moreover, created $e^+ - e^-$ pairs produced electrons that were hard to distinguish from trigger electrons. These sample contamination sources were accounted for and corrected as discussed in section 1.2.3. Still, a systematic error of the correction needs to be studied.

  To extract systematic uncertainties due to this source, ratios of the experimental to simulated data (see section 1.3.6) were found in two different ways. First, the "contamination" correction was applied to the inclusive data used to extract the trigger efficiency correction, and no "contamination" correction was applied to the tagged data themselves directly (only via the trigger efficiency correction). Second, no "contamination" correction was applied to the inclusive data, but it was rather applied directly to the tagged data. The difference between the two results was the systematic uncertainty on the ratio due to the "contamination" correction.

- **Choice of the inelastic simulation cross-normalization region.** As mentioned in section 1.3.6, the simulated inelastic tagged events were cross-normalized with the experimental data. For this, a specific region in W^* was chosen. The effect of the region on the final result had to be studied. For this, alternative normalization factors were obtained by multiplying the usual normalization factors by 0.95 (5% variation), and the calculation for the ratios was repeated using the alternative factors. The difference between the final results for the ratios obtained using these cross-normalization regions and usual ones (see section 1.3.6) was the systematic uncertainty due to the choice of the inelastic simulation cross-normalization region.

The systematic errors due to the aforementioned factors were added in quadrature, and the square root of this sum is shown on the plots as a point to point systematic error for the ratios of the experimental to simulated data. To convert these values to systematic errors of the F_{2n} structure function, they are multiplied by the value of model F_{2n} in the bin for which the error is calculated.

1.3.8 Sensitivity to Spectator Momentum

The main goal of this parallel analysis (MC method) has been to find the effective neutron structure function F_{2n}^{eff} as a function of p_s and θ_{pq} in different bins of W^* and Q^2, to check the validity of different FSI theories and the range of validity of the PWIA spectator picture in both spectator angle and momentum. Examples of our data are shown in figures 1.44 - 1.47. In the following, we discuss the dependence of ratios and extracted effective structure functions on p_s and $\cos\theta_{pq}$.

Fig. 1.44 shows the ratio of the experimental data with accidental background and elastic radiative tail subtracted to the simulated PWIA spectator model. The panels correspond to bins in spectator momentum with $p_s = 0.078$, 0.93, 0.11 and 0.135 GeV/c. Only backward-going spectators are included. At low p_s the ratio is close to unity for all W^* (except in the threshold region). Deviations at $W^* = 1.25$ and 1.50 GeV may reflect an underestimate of resonance strength in the model used in the simulation. With increasing p_s the deviations from unity grow substantially, indicating some combination of off-shell and FSI effects. The rise at low W^* is a remnant of the elastic tail, which may not have been completely subtracted (this could also be due to an incompletely simulated resolution effect, where the simulated data fall off more sharply as $W^* \rightarrow 1.08$, than the real ones).

Figure 1.45 shows F_{2n}^{eff}, which is produced by multiplying the ratio in Fig. 1.44 with F_{2n}^{model}. Here one can see the increasing deviation of the data from the model as p_s increases. This trend is consistent with the calculations of Ref. [12]) and the target fragmentation and FSI models of Refs. [13, 14] and [15]).

Fig. 1.46 shows the tagged event rate as a function of $\cos\theta_{pq}$, normalized by the Monte Carlo expectations from a pure spectator model. Deviations from unity indicate the effects of final-state interactions and off-shell effects. These data are at moderate Q^2 of 1.66 GeV^2, and $W^* = 1.73$ near the third resonance region. For $p_s = 0.078$ and 0.093 GeV, there is little indication of deviations from the spectator picture, even at forward angles. However, for

$p_s = 0.11$ and 0.135 GeV, still relatively low momenta, one finds a depletion perpendicular to the momentum transfer, which is a signature of final-state interactions, since the most likely np interaction is a grazing blow as the neutron moves largely in the direction of momentum transfer. This plot confirms that by limiting the spectator momenta to the range $0.07 < p_s < 0.1$ GeV, especially with a cut on backward angles, one observes a quasi-free neutron with small off-shell and final-state interaction corrections.

Fig. 1.47 shows F_{2n} as a function of x^*, again for $Q^2 = 1.66$ GeV^2, but for backward-going spectators with $-1 < \cos\theta_{pq} < -0.2$. There are only minor differences in F_{2n} as p_s increases from about 0.078 GeV (upper left) to 0.135 GeV (lower right). Especially in the deep-inelastic region, $W^* > 2$, there is no statistically significant evolution of the structure function with p_s. Hence, we can be confident that data with $0.07 < p_s < 0.10$ are not noticeably marred by either final-state interactions or off-shell effects.

1.3.9 Conclusions on the MC Analysis

The results shown tend to agree with the target fragmentation model of [13, 14] and the final state interaction model of [15]. Our data show an enhancement over PWIA in the target fragmentation region (in accordance with [13, 14]) and dip in the vicinity of $\theta_{pq} = 90°$ (in accordance with [15]).

The PWIA spectator model works well for the lowest two spectator momentum bins (p_s=70. . .100 MeV/c), as expected from the models of [16, 17] and [18, 19] especially in the backward θ_{pq} region, where deviations from PWIA are typically below 5–10%. The exceptions are the resonance peaks for the regions of $W^* \sim 1.25$ GeV and $W^* \sim 1.5$ GeV, where a resonance structure was evidently not described properly in the used model F_{2n}, and the deviation is close to 20%.

The resonance-like structure present in the ratio of the experimental data to the simulated data shows that our model for F_{2n} may underestimate the resonant contribution at some values of W^* and Q^2. On the other hand, the agreement between data and model for the 2 highest Q^2 bins and 5 GeV beam energy, over the whole range in W^*/x^*, is quite good in the region where the spectator picture should work (p_s between 0.07 and 0.085 GeV and $\cos(\theta_{pq})$ between -1 and -0.2) (see figure 1.48). This confirms that in the DIS region, the F_{2n} model provides a good description of a (nearly) free neutron up to $x^* \approx 0.6$, within our systematic errors of 10 - 15$\%$. This includes the systematic dependence on Q^2 for 5.254 GeV beam energy data (see figure 1.48). This dependence indicates that, for the neutron, the approach towards a universal (scaling) curve of $F_{2n}(x^*)$ (as expected from duality) does not yet seem to set in at the relatively low Q^2 where it was seen to hold in the proton case.

1.4 F_2^n and F_2^n/F_2^p Versus x

Fig. 1.49 shows a comparison of F_{2n} versus x^* obtained with the same data set, but the two alternative analysis methods. These points are summed over Q^2 for $W > 1.8$ GeV. They agree reasonably well with each other, and their deviations from each other can give an estimate of the differing systematic errors in the two methods.

Fig. 1.50 shows the final structure function ratio F_{2n}/F_{2p} versus x^* from the BoNuS experiment. Since this ratio does not evolve quickly with Q^2, we have included all Q^2 values above 1 GeV^2 in each x-bin. The different colored points show the effect of cutting into the resonance region where $W^* < 2$ GeV. If duality holds, the different Q^2 values contributing will wash out any resonance structure and we would expect the average ratio to follow the deep-inelastic trend. However, there is clearly an effect at $x = 0.65$, which corresponds to resonance structure around $W^* = 1.7$ GeV. The black points, and the off-resonance red points follow the CTEQ trend, suggesting that the n/p ratio may be taking “the middle road” in its asymptotic limit as $x \to 1$.

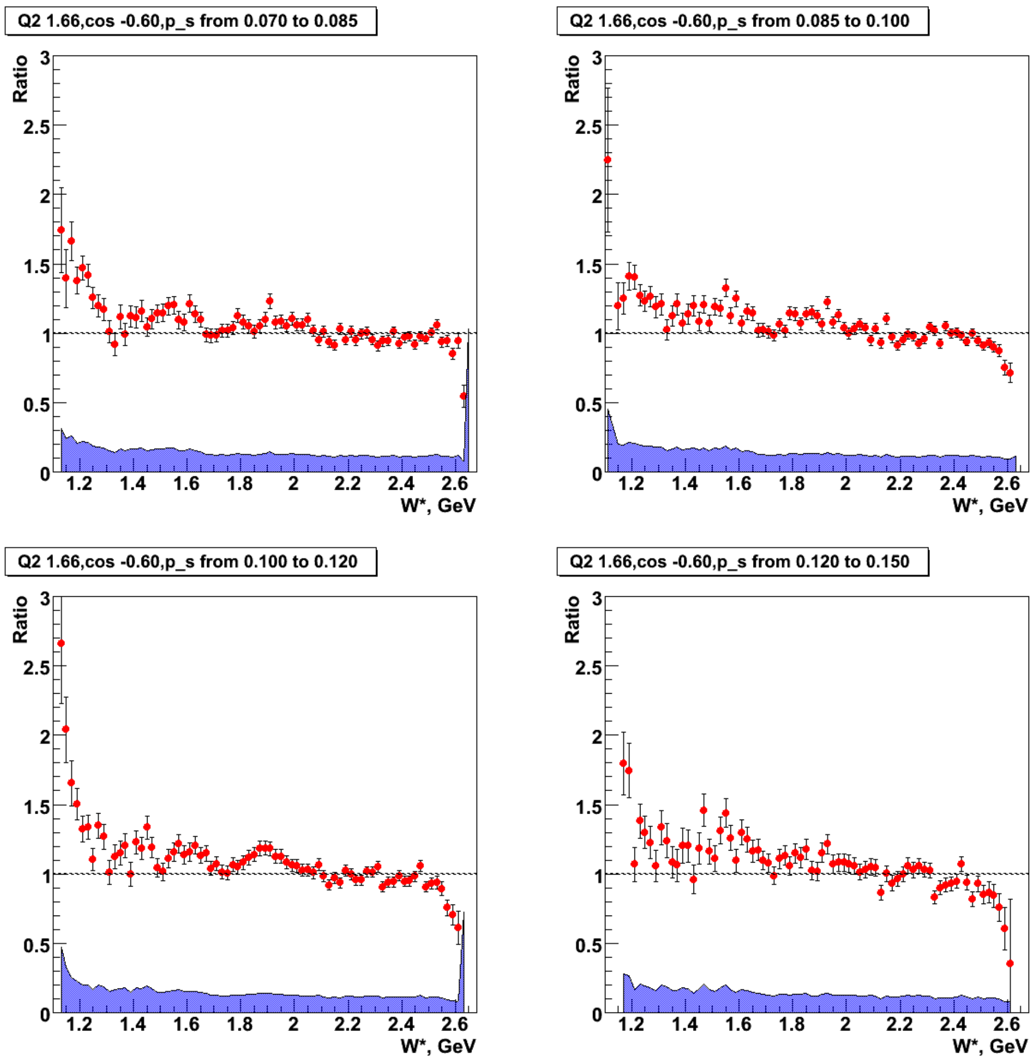

Figure 1.44: Ratio of experimental data with subtracted background and elastic tail to the full simulation in the PWIA spectator picture as a function of W^*. Data are for Q^2 from 1.10 to 2.23 $(\mathrm{GeV}/c)^2$ and $\cos\theta_{pq}$ from -1.0 to -0.2. The beam energy is 5.254 GeV. Error bars are statistical only. Systematic errors are shown as a blue band.

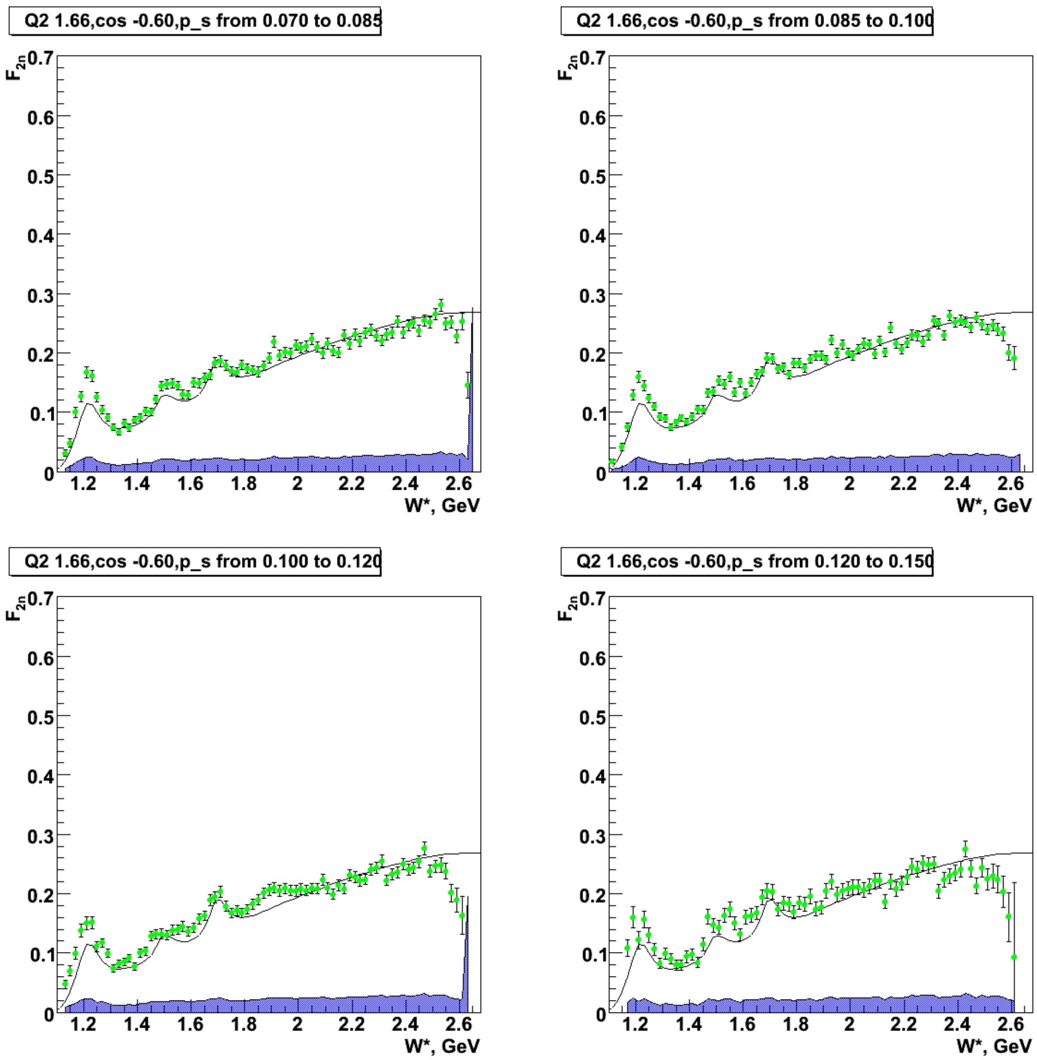

Figure 1.45: The effective F_{2n} structure function (green markers) is shown as a function of W^*. The black line is the model F_{2n} used in the simulation. Data are for Q^2 from 1.10 to 2.23 $(\mathrm{GeV}/c)^2$ and $\cos\theta_{pq}$ from -1.0 to -0.2. The beam energy is 5.254 GeV. Error bars are statistical only. Systematic errors are shown as a blue band.

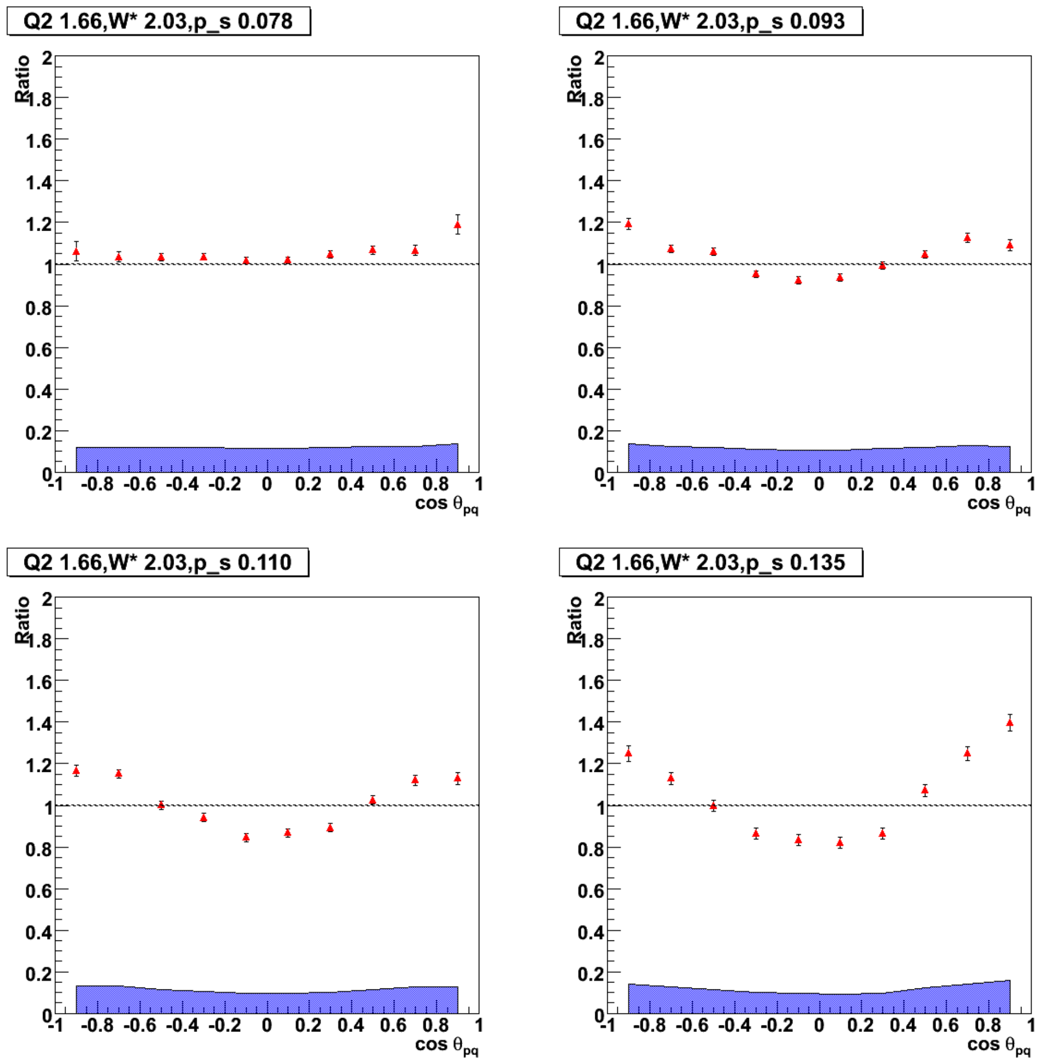

Figure 1.46: Ratio of experimental data with subtracted background and elastic tail to the full (normalized) simulation in the PWIA spectator picture is shown as a function of $\cos\theta_{pq}$. Data are for Q^2 from 1.10 to 2.23 (GeV$/c)^2$ and W^* from 1.85 to 2.2 GeV. The beam energy is 5.254 GeV. Error bars are statistical only. Systematic errors are shown as a blue band.

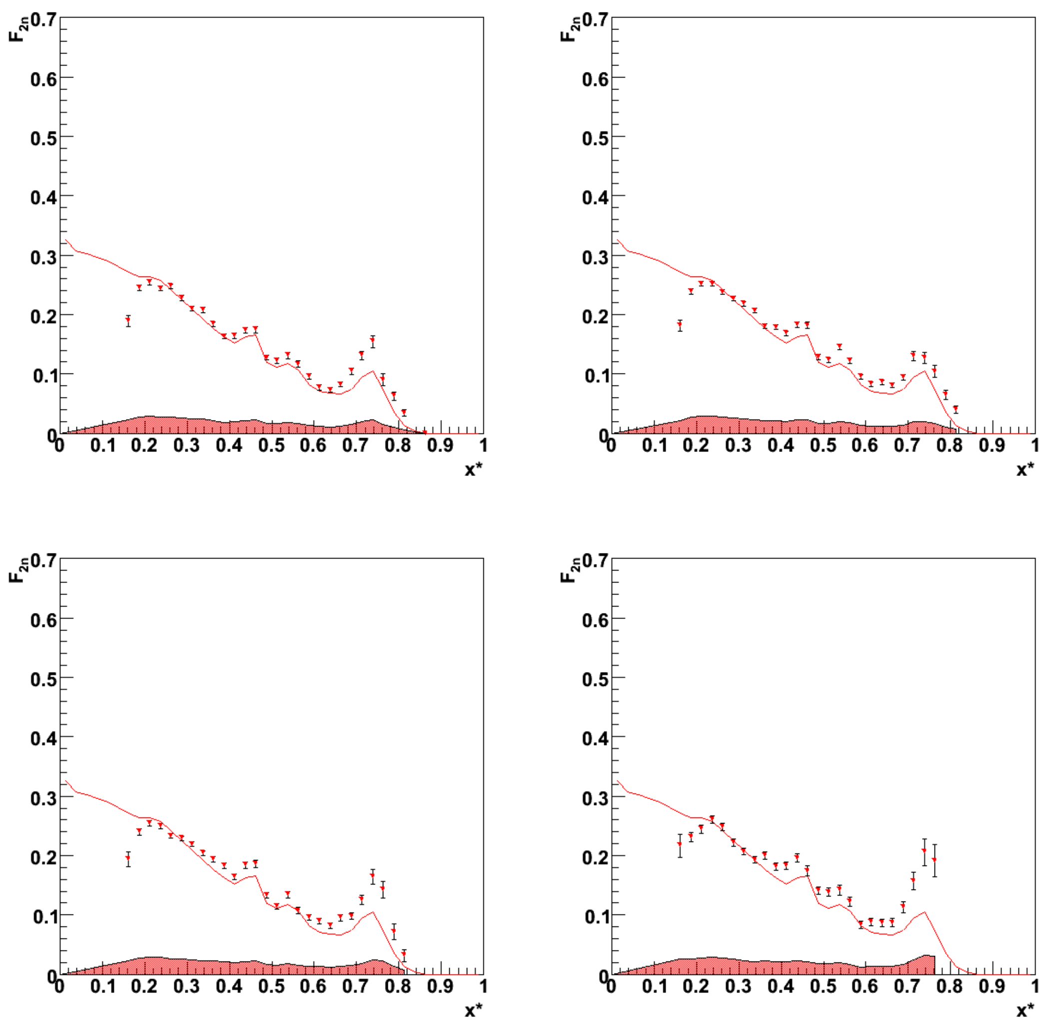

Figure 1.47: The effective F_{2n} structure function (green markers) is shown as a function of x^*. The red line is the model F_{2n}. Data are for Q^2 from 1.10 to 2.23 (GeV$/c)^2$ and $\cos\theta_{pq}$ from -1 to -0.2. The beam energy is 5.254 GeV. Error bars are statistical only. Systematic errors are shown as a blue band.

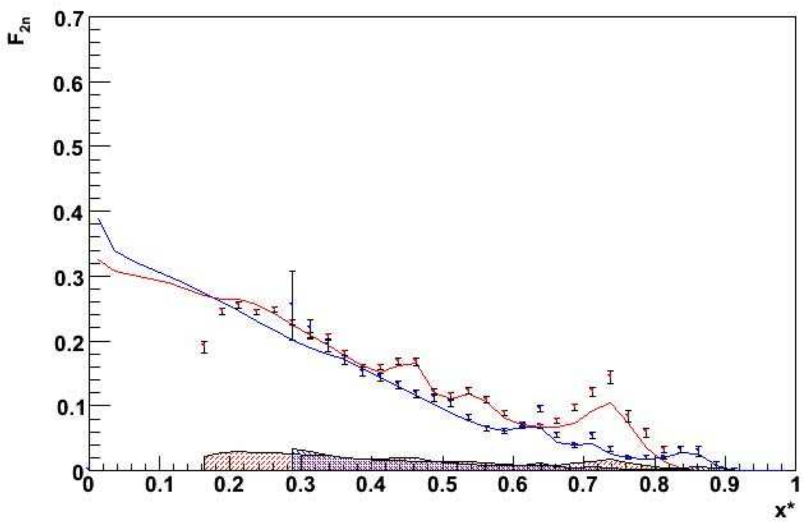

Figure 1.48: Model F_{2n} (lines) and measured effective F_{2n} (markers) are shown as functions of x^* for two Q^2 bins: from 1.10 to 2.23 $(\mathrm{GeV}/c)^2$ (red) and from 2.23 to 4.52 $(\mathrm{GeV}/c)^2$ (blue). Results are shown for backward angles ($\cos(\theta_{pq})$ between -1.0 and -0.2) and low spectator momenta (p_s between 70 and 85 MeV/c), for which the spectator model should be a good description. The beam energy is 5.254 GeV.

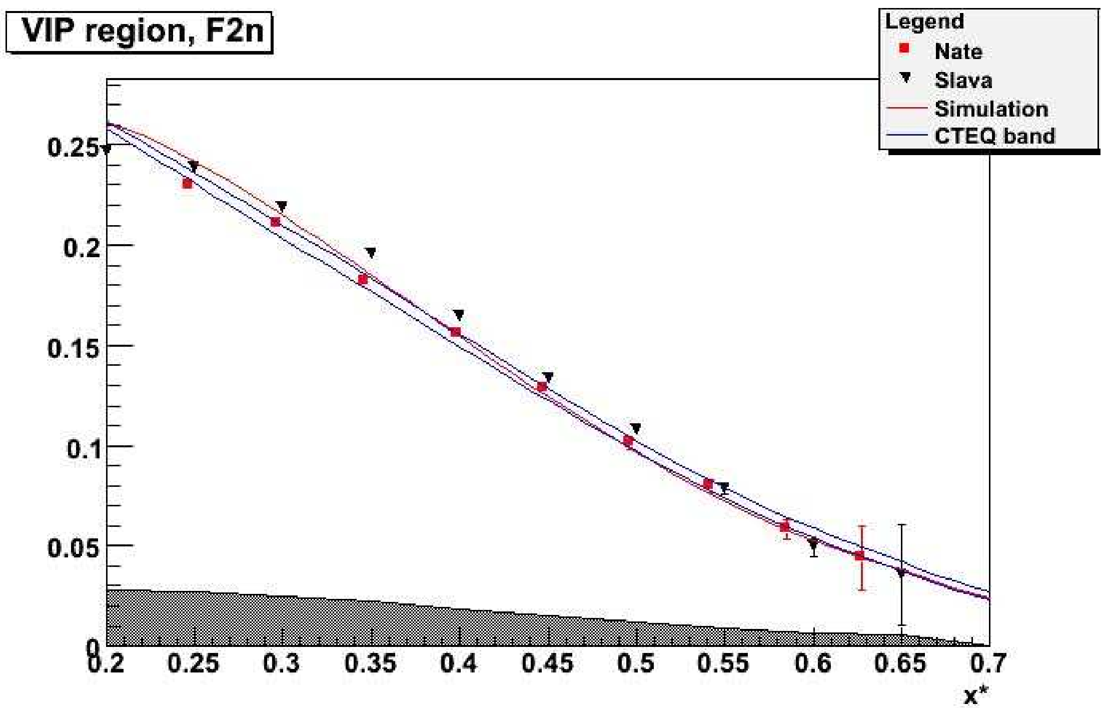

Figure 1.49: The BoNuS experimental F_{2n} versus x derived from the two independent analyses of the same data set. Red points ("Nate") correspond to the tagged/untagged ratio method and blue points ("Slava") correspond to the tagged to Monte Carlo ratio method. The blue lines indicate the uncertainty limits of the CTEQ6x fit (see below), while the red line is from the fit used in our Monte Carlo simulation. The two methods agree reasonably well - the differences in all cases are smaller than the quoted systematic error (including the difference due to different normalization prescriptions).

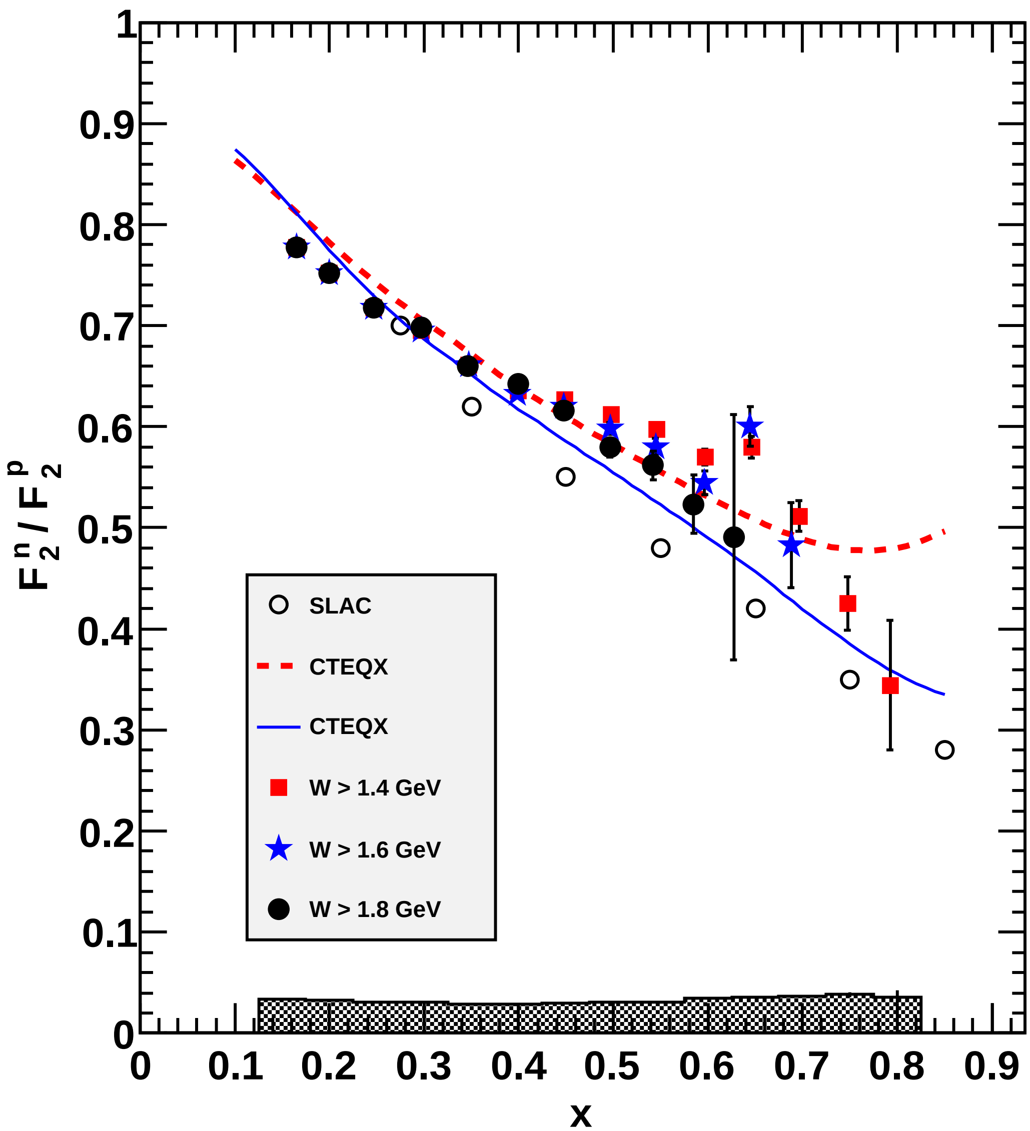

Figure 1.50: The ratio F_2^n/F_2^p versus x. The SLAC deuteron data (circles) are from [20] and [21], with corrections for Fermi motion only (blue curve) or for point-like nucleon configurations based on Ref. [22]. The dashed red and the solid blue curves correspond to the upper and lower bounds on this ratio from the CETQ global structure function fit for high x. The BoNuS data are from the E_{beam} =5.262 GeV run period, with statistical uncertainties shown on the points and total (correlated) systematic uncertainties shown in the error band on the bottom of plot. The colored points indicate cuts on W^* above 1.4 GeV (red), 1.6 GeV (blue) and 1.8 GeV (black).

BIBLIOGRAPHY

[1] A. V. Klimenko *et al.*, “Electron scattering from high-momentum neutrons in deuterium,” *Phys. Rev.*, vol. C73, p. 035212, 2006.

[2] K. Abe *et al.*, “Measurements of the proton and deuteron spin structure functions g1 and g2,” *Phys. Rev.*, vol. D58, p. 112003, 1998.

[3] J. Arrington, C. D. Roberts, and J. M. Zanotti, “Nucleon electromagnetic form factors,” *J. Phys.*, vol. G34, pp. S23–S52, 2007.

[4] M. E. Christy and P. E. Bosted, “Empirical Fit to Precision Inclusive Electron-Proton Cross Sections in the Resonance Region,” *arXiv:0712.3731*, 2007.

[5] P. E. Bosted and M. E. Christy, “Empirical Fit to Inelastic Electron-Deuteron and Electron-Neutron Resonance Region Transverse Cross Sections,” *Phys. Rev.*, vol. C77, p. 065206, 2008.

[6] L. Mo and Y. Tsai, “Radiative Corrections to Elastic and Inelastic ep and μp Scattering,” *Rev. Mod. Phys.*, vol. 41, p. 205, 1969.

[7] M. Lacombe *et al.*, “Parametrization of the deuteron wave function of the Paris n-n potential,” *Phys. Lett.*, vol. B101, pp. 139–140, 1981.

[8] M. Lacombe *et al.*, “Parametrization of the Paris n n Potential,” *Phys. Rev.*, vol. C21, pp. 861–873, 1980.

[9] S. J. Brodsky, “Light-cone quantized QCD and novel hadron phenomenology,” 1997.

[10] M. Arneodo *et al.*, “Measurement of the proton and the deuteron structure functions, F2(p) and F2(d),” *Phys. Lett.*, vol. B364, pp. 107–115, 1995.

[11] S. Agostinelli *et al.*, “GEANT4: A simulation toolkit,” *Nucl. Instrum. Meth.*, vol. A506, pp. 250–303, 2003.

[12] W. Melnitchouk, M. Sargsian, and M. I. Strikman, "Probing the origin of the EMC effect via tagged structure functions of the deuteron," *Z. Phys.*, vol. A359, pp. 99–109, 1997.

[13] C. Ciofi degli Atti and S. Simula, "Slow proton production in semiinclusive deep inelastic lepton scattering off nuclei," *Phys. Lett.*, vol. B319, pp. 23–28, 1993.

[14] S. Simula, "Semi-inclusive deep inelastic electron scattering off the deuteron and the neutron to proton structure function ratio," *Phys. Lett.*, vol. B387, pp. 245–252, 1996.

[15] C. Ciofi degli Atti, L. P. Kaptari, and B. Z. Kopeliovich, "Hadronization and final state interaction effects in semi- exclusive deep inelastic scattering off nuclei," *Eur. Phys. J.*, vol. A19, pp. 133–137, 2004.

[16] W. Melnitchouk, A. W. Schreiber, and A. W. Thomas, "Relativistic deuteron structure function," *Phys. Lett.*, vol. B335, pp. 11–16, 1994.

[17] W. Melnitchouk, A. W. Schreiber, and A. W. Thomas, "Deep inelastic scattering from off-shell nucleons," *Phys. Rev.*, vol. D49, pp. 1183–1198, 1994.

[18] F. Gross and S. Liuti, "Role of nuclear binding in the EMC effect," *Phys. Rev.*, vol. C45, pp. 1374–1381, 1992.

[19] S. Liuti and F. Gross, "Extraction of the ratio of the neutron to proton structure functions from deep inelastic scattering," *Phys. Lett.*, vol. B356, pp. 157–162, 1995.

[20] L. Whitlow *et al.*, "Precise measurements of the proton and deuteron structure functions from a global analysis of the SLAC deep inelastic electron scattering cross sections," *Phys. Lett. B*, vol. 282, p. 475, 1992.

[21] J. Gomez *et al.*, "Measurement of the a dependence of deep-inelastic electron scattering," *Phys. Rev. D*, vol. 49, pp. 4348–4372, May 1994.

[22] W. Melnitchouk and A. W. Thomas, "Neutron / proton structure function ratio at large x," *Phys. Lett.*, vol. B377, pp. 11–17, 1996.